

Wideband High-Gain mm-wave MIMO Antenna Design for 5G IoT Applications

Hassan Zakeri, Gholamreza Moradi, *Senior Member, IEEE*, Mohammad Alibakhshikenari, *Member, IEEE*, Bal S. Virdee, *Senior Member, IEEE*, Chan Hwang See, *Senior Member, IEEE* and, Slawomir Koziel, *Fellow, IEEE*

Abstract—A compact four-port (2×2) millimeter-wave (mm-wave) microstrip MIMO antenna front-end is presented for 5G New Radio (NR) Internet of Things (IoT) edge and aerial connectivity in the FR2 bands. Rather than serving as a standalone electromagnetic structure, the proposed design targets short- to medium-range IoT gateway and UAV-assisted deployment scenarios where front-end hardware performance directly governs achievable link reliability and coverage. The antenna integrates a flower-shaped radiator with an evolved defected ground structure (DGS) combining a circular complementary split-ring resonator (CSRR), rotated rectangular slots, and cross-elliptical slots to achieve a wide impedance bandwidth, high realized gain, and strong inter-element isolation without multilayer superstrates or external decoupling networks. Fabricated on a 0.508-mm-thick Rogers RT/Duroid@5880 substrate with an overall footprint of $37.7 \times 37.7 \text{ mm}^2$, the antenna covers the 5G NR n258 (24.25–27.50 GHz) and n257 (26.50–29.50 GHz) bands, providing an aggregate impedance bandwidth of approximately 13.5 GHz. Measured results demonstrate a peak realized gain of 9.8 dBi, average gain of approximately 8.7 dBi across the operating band, radiation efficiency between 85%–88%, and inter-port isolation exceeding 26 dB. Excellent MIMO performance is achieved with an envelope correlation coefficient (ECC) below 0.002, diversity gain close to 10 dB, and low channel capacity loss. Beyond antenna characterization, a deployment-oriented link-budget analysis grounded in measured gain and efficiency, together with large-scale path loss modeling, is performed to translate the validated hardware performance into achievable link margins under realistic FR2 propagation conditions. The results confirm that the proposed MIMO front-end provides sufficient link feasibility for compact, high-capacity 5G mm-wave IoT edge devices operating in dense and aerial deployment environments.

Index Terms—5G antenna, Defected ground surface, Internet of Things, mm-wave, MIMO, New radio

H. Zakeri and G. Moradi are with the Department of Electrical Engineering, Amirkabir University of Technology (Tehran Polytechnic), Iran, Tehran 15875-4413 (e-mail: h.zakeri@aut.ac.ir; ghmoradi@aut.ac.ir).

Mohammad Alibakhshikenari is with Lero, the Research Ireland Centre for Software, College of Science and Engineering, School of Computer Science, University of Galway, H91 TK33 Galway, Ireland. He is also with the Department of Electrical and Electronics Engineering, Dogus University, 34775 Umraniye, Istanbul, Türkiye (e-mail: mohammad.alibakhshikenari@universityofgalway.ie)

Bal S. Virdee is with Center for Communications Technology, London Metropolitan University, N7 8 DB London, U.K. (e-mail: b.virdee@londonmet.ac.uk)

Chan Hwang See is with School of Computing, Engineering and the Built Environment, Edinburgh Napier University, 10 Colinton Road, Edinburgh, EH10 5DT, United Kingdom (e-mail: c.see@napier.ac.uk)

Slawomir Koziel is with the Faculty of Electronics, Telecommunication and Informatics, Gdańsk University of Technology, 80-233 Gdańsk, Poland, and also with the Department of Engineering, Reykjavik University, 102 Reykjavik, Iceland (e-mail: slakoziel@pg.edu.pl)

I. INTRODUCTION

Recent progress in fifth-generation (5G) New Radio (NR) systems and wireless communication technologies has attracted significant research attention. High-performance wireless devices with compact RF front ends and antennas are increasingly essential to enable seamless operation across use cases such as device-to-device (D2D) communication, virtual/augmented reality, the Internet of Things (IoT), telemedicine, smart homes, smart farming, and innovative industry [1]–[3].

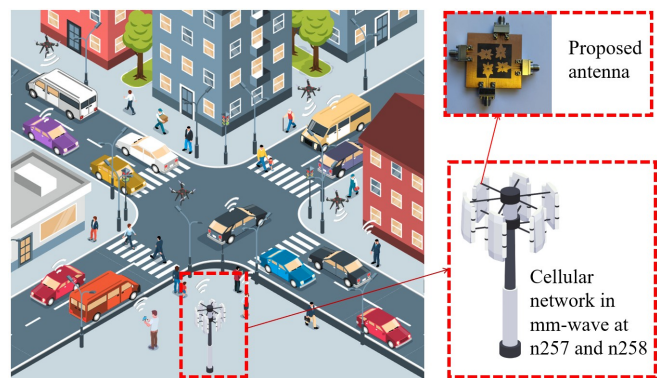


Fig. 1: Conceptual illustration of a 5G-enabled smart-city IoT environment highlighting potential use cases for the proposed antenna (not an experimental deployment).

As more users access the internet through diverse wireless devices, networks must support higher data rates with lower latency, which raises the design complexity of the underlying hardware and propagation solutions [4]–[7]. The fusion of 5G with IoT and artificial intelligence is expected to accelerate this trend and catalyze smart cities, advanced healthcare, precision agriculture, automated manufacturing, intelligent transportation systems (ITS), and immersive XR applications [8], [9]. A standard 5G network is demonstrated in Fig. 1.

Market forecasts further underscore the scale of the opportunity: Intel projects a \$6.2-trillion IoT market by 2025 and an installed base of ~ 38 billion connected devices by end-2025, rising to ~ 50 billion by 2030 [1], [10].

These devices span multiple 5G frequency allocations, with 28 GHz and 38 GHz particularly attractive due to their support for high data rates, lower absorption in specific windows, and broad (partly unlicensed) BW availability [11], [12]. However, compared with sub-6 GHz, millimeter-wave (mm-wave) bands suffer higher atmospheric and propagation losses.

Consequently, narrow-beam, high-gain antennas are required to overcome attenuation and link budget deficits in mm-wave IoT deployments, thereby tightening the constraints on antenna architecture, footprint, and integration [13]–[15].

Multiple techniques have been explored to increase antenna gain, including lens-coupled apertures, dielectric resonator antennas (DRAs), superstrate-loaded patches, and stacked-substrate configurations [16], [17]. While effective, these approaches often involve complex geometries and thicker, non-planar profiles that complicate device-level integration.

Planar antenna arrays are easier to co-design with electronics [18]–[20], but arraying alone increases footprint and does not directly address channel capacity. In contrast, multiple-input multiple-output (MIMO) architectures exploit multipath to raise data rates and capacity at constant transmit power, and are therefore central to 5G radio links [21]–[23]. A broad mm-wave literature spans single-port, array, and MIMO solutions for 5G applications [24]–[26]; nonetheless, single-port and simple arrays are insufficient on their own to ensure robust mm-wave connectivity under mobility and blockage. Numerous MIMO antennas have been reported [25], [27]–[29], yet many designs face trade-offs among BW, isolation, gain, and size. For example, a three-port antenna of $55 \times 110 \times 1.66 \text{ mm}^3$ achieves only 4.6 dBi peak gain with 1.3 GHz BW over 37.3–38.6 GHz [30]. A four-port MIMO with 34 dB isolation offers just 0.35 GHz BW from 38.02 to 38.37 GHz [31]. Another four-port system ($158 \times 77.8 \times 0.381 \text{ mm}^3$) spans 27.5–40 GHz with 7.2 dBi peak gain and >17 dB isolation [28]. A similar four-element MIMO ($26.6 \times 3.25 \times 1.6 \text{ mm}^3$) provides 0.64 GHz BW (36.68–37.32 GHz) and 5.2 dBi gain [32]. A two-element MIMO reports 21 dB isolation and 1.83 dBi peak gain over 36.95–39.05 GHz [33]. A DGS-based four-element MIMO for 25.5–29.6 GHz attains 8.3 dBi peak gain over 4.3 GHz BW, yet underscores the difficulty of jointly optimizing wideband behavior, isolation, gain, and compactness [34]. Overall, prior work indicates that MIMO antennas with full ground planes and linear orientations often struggle to achieve adequate port isolation, and balancing wide BW, low coupling, competitive gain, and small size remains challenging.

Defective ground structures (DGS) and electromagnetic bandgap (EBG) structures have been integrated into hybrid approaches to reduce coupling and enhance performance, as have slots and parasitic elements [35]. Additional techniques include zigzag ground slots [34], half ring slots [36], partially reflecting surfaces [37], partial grounds [38], partial grounds with metasurfaces [39], ground-plane slotting [40], [41], decoupling branches [42], and decoupling networks [43]. Metamaterial-based EBGs and frequency-selective surfaces (FSSs) can further increase gain, but typically at a substantial size penalty. Many of these solutions require multi-stage fabrication and tight tolerances; at mm-wave scales, such complexity becomes increasingly impractical.

Although connected-ground MIMO configurations have been widely investigated [44]–[46], achieving high isolation between closely spaced elements remains challenging, thereby limiting the overall system capacity.

Several representative mm-wave MIMO examples illustrate

these trade-offs. A metasurface-based four-port array with a corporate feed on Rogers RT/Duroid®5880 measures $43 \times 30 \times 0.78 \text{ mm}^3$, but its intricate construction and $\sim 2 \text{ GHz}$ BW reduce suitability for compact wireless devices [47]. An FSS-assisted MIMO ($18 \times 19 \times 0.8 \text{ mm}^3$) resonates at 28 GHz with 1.6 GHz total BW (27.25–28.85 GHz); an added FSS ($7 \times 7 \text{ mm}^2$ unit cells; $45 \times 45 \text{ mm}^2$ overall) improves gain and isolation to 8.6 dBi and 23.31 dB, respectively, at the expense of extra volume [48]. A compact monopole wideband antenna ($40 \times 20 \times 1.52 \text{ mm}^3$) augmented by an FSS ($10 \times 10 \text{ mm}^2$ unit cells; $58 \times 38 \text{ mm}^2$ overall) increases gain to 4.5 dBi but again enlarges the design [49]. Two quad-element UWB antennas for IoT demonstrate small size and solid performance, yet they target short-range links with limited data rates [50], [51]. In summary, the state of the art faces persistent issues such as intricate structures, constrained BW, inadequate isolation, and size/gain trade-offs, highlighting the need for mm-wave MIMO solutions that are simultaneously compact, wideband, high-gain, and low-coupling.

To address these gaps, we present a compact, flower-shaped, four-port MIMO antenna for 5G NR IoT implemented on Rogers RT/Duroid®5880 with an overall footprint of $37.7 \times 37.7 \text{ mm}^2$. The design covers the mm-wave bands n257 (26.50–29.50 GHz) and n258 (24.25–27.50 GHz) and employs a separate-ground configuration to enhance isolation while maintaining a low profile and small area. An evolved DGS integrates a circular CSRR with three rotated rectangular slots and cross-shaped elliptical slots, placed beneath the feedline-patch junction, to tune and broaden the operating bands by maximizing the BW center frequency. The radiating patches are oriented orthogonally to mitigate mutual coupling and further compress the footprint. Beyond S-parameters and gain, the antenna is evaluated using MIMO-specific and time-domain metrics, including the envelope correlation coefficient (ECC), mean effective gain (MEG), diversity gain (DG), group delay, link budget analysis, and channel capacity loss (CCL) to validate robust link performance under realistic multipath conditions.

In contrast to many recent wideband mm-wave MIMO antennas that rely on external metasurfaces, electromagnetic bandgap structures, partially reflecting superstrates, or multilayer assemblies to enhance gain and isolation, the proposed design achieves its performance solely through planar-radiator shaping and single-layer ground-plane engineering. The combined use of a flower-shaped radiator and a CSRR-loaded evolved DGS enables simultaneous BW enhancement, gain improvement, and mutual-coupling suppression without additional volume, vias, or alignment-sensitive layers. Consequently, the proposed antenna offers a more favorable performance-complexity trade-off, particularly for compact 5G IoT devices where fabrication simplicity, low profile, and ease of integration are critical.

This work presents a hardware-enabling mm-wave MIMO front-end solution targeting high-density IoT edge nodes operating in 5G NR FR2 bands. In emerging mm-wave IoT ecosystems, front-end antenna performance directly constrains achievable link margin, spatial multiplexing capability, and integration feasibility. Accordingly, this study combines fab-

ricated hardware validation, comprehensive MIMO-domain characterization, and deployment-oriented link feasibility analysis to demonstrate practical IoT relevance grounded in experimentally measured performance. Physical-layer hardware innovations play a foundational role in enabling reliable IoT edge connectivity at FR2 frequencies. Compared to sub-6 GHz systems, mm-wave operation introduces significantly higher free-space attenuation, increased blockage sensitivity, and reduced diffraction capability. These propagation constraints are further compounded in compact IoT devices, where limited footprint, low-profile integration, and electromagnetic compatibility requirements restrict antenna design flexibility. Unlike conventional mobile broadband terminals, IoT edge platforms—such as industrial sensor gateways, UAV-assisted monitoring systems, and dense smart-factory nodes—operate under strict size, power, and integration constraints while requiring stable, short- to medium-range high-capacity connectivity. In such scenarios, wideband, high-isolation MIMO antenna architectures become critical for supporting reliable sensing, monitoring, and control links under multipath and partial blockage conditions. The proposed compact four-port mm-wave MIMO antenna is developed specifically with these IoT-oriented deployment constraints in mind. Its single-layer planar structure facilitates integration into space-limited IoT platforms, while the evolved defected ground structure (DGS) and orthogonal element configuration provide strong inter-port isolation and extremely low envelope correlation. These features enhance diversity performance and link robustness, supporting high-capacity IoT edge connectivity in the 5G NR n257/n258 bands.

The primary contributions of this work are summarized as follows:

- 1) A compact wideband mm-wave MIMO front-end is developed to operate in the 5G NR n257 and n258 bands, addressing the integration and propagation challenges associated with FR2 IoT edge platforms such as industrial gateways and aerial sensing nodes.
- 2) A four-port antenna configuration is introduced that achieves strong inter-port isolation and extremely low envelope correlation coefficient (ECC), enabling reliable multi-stream communication in densely deployed IoT environments where antenna elements must operate within a limited footprint.
- 3) A single-layer antenna architecture incorporating an evolved defected ground structure with complementary split ring resonator loading and slot engineering is proposed to enhance bandwidth, gain, and isolation without the need for multilayer structures or external superstrates, improving practical integration in space-constrained IoT devices.
- 4) The fabricated prototype is experimentally characterized through measurements of realized gain, radiation efficiency, radiation patterns, and key MIMO performance metrics including ECC, diversity gain (DG), mean effective gain (MEG), and channel capacity loss (CCL), demonstrating stable performance under multipath-sensitive mm-wave propagation conditions.

- 5) A deployment-oriented link-budget analysis is conducted using experimentally measured antenna parameters combined with large-scale path-loss modelling to quantify achievable link margins and communication feasibility for representative short- to medium-range FR2 IoT edge connectivity scenarios.

In summary, this work develops a compact, integration-friendly mm-wave MIMO antenna front-end that simultaneously achieves a wide impedance bandwidth, high realized gain, and low inter-element coupling for 5G NR IoT platforms. The proposed architecture combines a flower-shaped radiator with an evolved defected-ground structure incorporating CSRR loading and engineered slot configurations to enhance bandwidth and isolation without increasing structural complexity. Orthogonal element placement further improves diversity performance, while equivalent-circuit modeling provides insight into the underlying operating mechanism. Together with measured validation and deployment-oriented feasibility evaluation, the results demonstrate the suitability of the proposed MIMO front-end for reliable, high-capacity mm-wave IoT edge connectivity.

The remainder of the paper is organized as follows. Section II details the antenna geometry and design evolution. Section III presents parametric analysis. Section IV reports final simulated and measured results. Section V discusses MIMO characteristics. Sections VI and VII present time-domain and link budget analyses, respectively. Section VIII analyzes the path loss of the proposed structure mounted on the drone. Finally, Section X concludes the work.

II. ANTENNA DESIGN METHODOLOGY

A. Geometric configuration

The top and bottom layouts of the single antenna element are depicted in Figs. 2(a) and 2(b), which are then expanded to a four-element MIMO antenna configuration.

The radiating patch is excited by a feedline with width W_f and length L_f . To achieve good impedance matching and reduce the reflection coefficient, a triangular microstrip is used to connect the patches to the feed line [52]. Two cross-rectangular slots are used on top of the single element, which is made up of six elliptical petals. The suggested structure uses a CSRR and three rectangular slots that are rotated $\theta_t = 42^\circ$ degrees at the bottom.

The antenna is fabricated on Rogers RT/Duroid@5880 substrate with relative permittivity $\epsilon_r = 2.2$, dielectric loss tangent $\tan\delta = 0.0009$, and substrate thickness $h = 0.508$ mm. The low loss tangent helps maintain high radiation efficiency and realized gain at millimeter wave frequencies. Additionally, the proposed antenna's overall dimension is 37.7×37.7 mm². All simulation results shown below were obtained using the electromagnetic simulator CST Microwave Studio. The low $\tan\delta$ helps preserve realized gain and efficiency in the 24–30 GHz range, while the low permittivity improves radiation efficiency and BW by reducing dielectric loading. The thin 0.508-mm substrate further mitigates surface-wave excitation and parasitic coupling, thereby improving impedance matching and consistent radiation performance across the operating

band. These properties make Rogers RT/Duroid@5880 well-suited for compact, planar mm-wave MIMO antennas intended for practical integration into 5G IoT hardware.

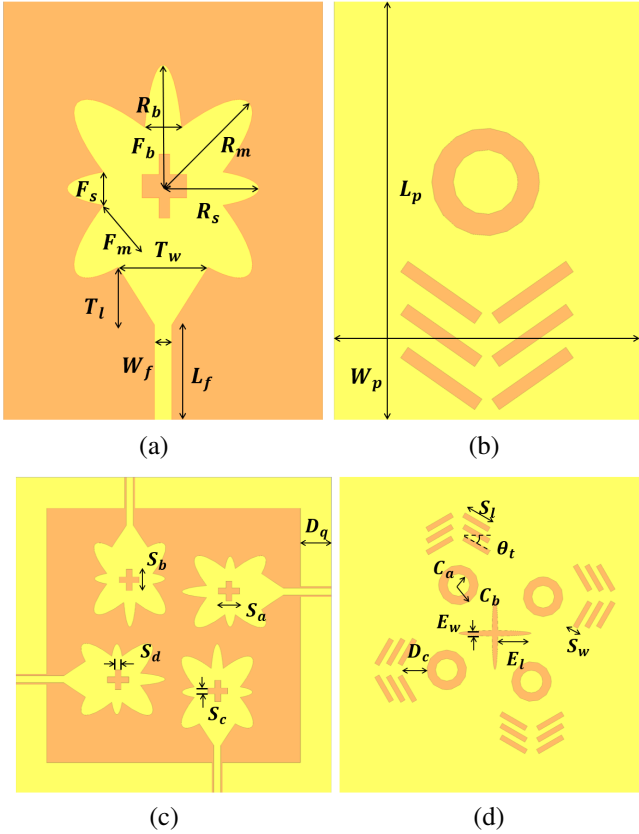


Fig. 2: Single antenna element: (a) top view, (b) bottom view, and four-port MIMO antenna: (c) top view, (d) bottom view.

Figs. 2(c) and 2(d) present the top and bottom views of the final four-port MIMO design $37.7 \times 37.7 \text{ mm}^2$. The ground plane, equal in size to the substrate, incorporates symmetrically etched orthogonal elliptical slots Fig. 2(d) and serves to confine backward radiation and enhance performance. Table I provides a detailed list of the single element's dimensions. Initial values were obtained from the well-known transmission-line model for circular microstrip patches [53].

The geometry of the proposed antenna is derived through a structured and physically guided design process rather than arbitrary shaping. The top metallization of each antenna element consists of a modified circular microstrip patch, transformed into a flower-shaped radiator by attaching six symmetrically arranged elliptical petals around a central circular core. These petals extend the effective surface-current path, thereby lowering the resonant frequency and generating multiple closely spaced resonances that contribute to a wide impedance BW without increasing the overall footprint. Two orthogonally crossed rectangular slots are etched into the radiating patch to tune the input impedance further and stabilize broadband matching. The radiator is excited by a microstrip feed line connected via a triangular taper, ensuring a smooth impedance transition between the feed and the radiating aperture.

The bottom layer comprises a continuous ground plane that incorporates an evolved defected ground structure (DGS). A circular complementary split-ring resonator (CSRR) is etched directly beneath the feedline-patch junction to introduce a controlled LC resonance that enhances BW and supports partial miniaturization. In addition, three rectangular slots rotated by an angle of $\theta = 45^\circ$ are etched around the CSRR to adjust the local ground impedance and flatten the impedance response over the operating band. To suppress surface-wave coupling between adjacent elements, cross-shaped elliptical slots are symmetrically etched in the ground plane, redirecting surface currents away from neighboring feeds and significantly improving inter-element isolation.

The single antenna element is extended to a four-port (2×2) MIMO configuration by placing four identical radiators orthogonally within the same substrate footprint. This orthogonal orientation inherently reduces polarization and pattern correlation, while the shared ground plane with the evolved DGS further suppresses mutual coupling. All geometric parameters are initially estimated using classical transmission-line and cavity-model formulations for circular microstrip antennas and are subsequently optimized through full-wave parametric analysis to achieve the final trade-off among impedance BW, gain, and isolation.

B. Proposed Design Equations

The four-port MIMO antenna comprises four radiators, each excited by a simple microstrip feed line. All radiating elements were dimensioned using analytical formulas. For the circular microstrip patches, the single-element (unit-cell) dimensions, such as patch radius and feed parameters, were obtained from standard closed-form equations [54], [55] derived from the cavity model of a circular microstrip antenna. These analytical formulations provide a starting point for determining the fundamental geometric parameters of the radiator before full wave numerical optimization. The resonant frequency of a circular microstrip patch operating in dominant TM_{11} mode can be approximated as

$$f_r = \frac{c}{2a_e \sqrt{\epsilon_r}} \quad (1)$$

where f_r is the desired resonant frequency, c indicates the speed of light, ϵ_r indicates the relative permittivity of the dielectric substrate and a_e is the effective radius of the circular patch due to fringing fields at the patch edge. The physical radius a of the circular patch can be calculated as:

$$a = \frac{F}{\sqrt{1 + \frac{2h_t}{\pi F \epsilon_r} [\ln(\frac{\pi F}{2h_t}) + 1.7726]}} \quad (2)$$

$$F = \frac{8.791 \times 10^9}{f_r \sqrt{\epsilon_r}} \quad (3)$$

$$a_e = a \left(\sqrt{1 + \frac{2h_t}{\pi \epsilon_r a} [\ln(\frac{\pi a}{2h_t}) + 1.7726]} \right) \quad (4)$$

where F is the intermediate parameter and h_t is the substrate height.

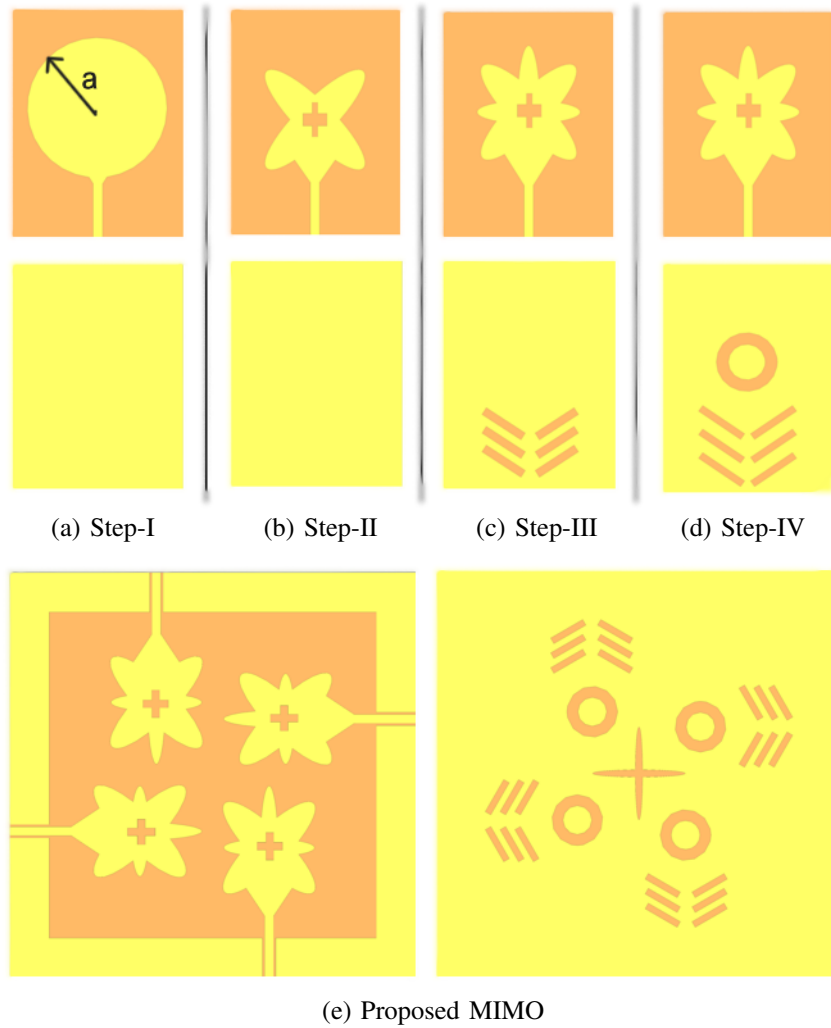


Fig. 3: Design evolution of the single-element antenna and MIMO configuration, where a in Fig. 3(a) is the circular patch radius used in the analytical resonant frequency calculation.

The analytical expressions presented in this section determine the initial values for the fundamental patch parameters, including the effective patch radius, substrate thickness, and feed position, which set the baseline resonant frequency and input impedance. These equations are directly linked to the primary geometric features shown in Fig. 3(a), such as the circular patch radius and feed-line dimensions. In contrast, the flower-shaped petal extensions, crossed rectangular slots, and the CSRR with rotated ground slots cannot be derived analytically due to their higher-order electromagnetic interactions; therefore, their dimensions are established and refined through full-wave parametric optimization in Section III. Together, the analytical starting point and numerical refinement lead to the final optimized geometry.

C. Evolution of the Proposed Structure and Operating Principle

Fig. 3 illustrates the evolution of the antenna from a single modified circular patch to a four-port MIMO array and the associated performance improvements. The dimensions and

TABLE I: Parameters of the proposed MIMO structure.

Parameter	Value (mm)	Parameter	Value (mm)
R_b	5.4	L_p	19.6
R_m	5.6	W_p	14.2
R_s	4.1	L_f	4.8
F_b	1.4	W_f	0.8
F_m	2.9	T_w	4.1
F_s	1.2	T_l	2.5
S_a	2.2	S_l	4.2
S_b	2.9	S_w	0.6
S_c	0.8	E_l	4.6
S_d	0.7	E_w	0.4
D_q	3.6	D_c	3.4
C_a	1.5	C_b	2.4
θ_t	42°	H_s	0.508

incremental modifications are chosen to enhance impedance matching and gain.

The antenna design is developed through a progressive geometry evolution process. The initial configuration consists of a circular microstrip patch, as shown in Fig. 3(a), where the patch radius is determined using the analytical resonant

frequency formulation. In this stage, the patch dimension is selected to be comparable to the feedline length. Subsequent modifications, including downward extensions and slot engineering, are introduced to improve impedance matching and enhance the antenna gain.

Two symmetrical, petal-shaped expanded patches that are almost as wide as the radiator are added in Step-II (Fig. 3(b)). As illustrated in Fig. 4(a), this device resonates at 34.740 GHz with a wide-band response and poor impedance matching. Additionally, Fig. 4(b) validates gain augmentation.

At Step III, the final top patch shape is proposed. This structure in the ground layer features three pairs of rotated slots that enhance BW and improve impedance matching.

The final suggested form with an adjustable cross slot at the top of the patch and CSSR is added in Step IV (see Fig. 3(c)). At this point, the design performs satisfactorily. It does not, however, address the data rate problem as outlined in 5G regulations. The design is expanded to a MIMO arrangement, where antenna elements are positioned orthogonally to one another, as illustrated in Fig. 4(d), to increase the data rate.

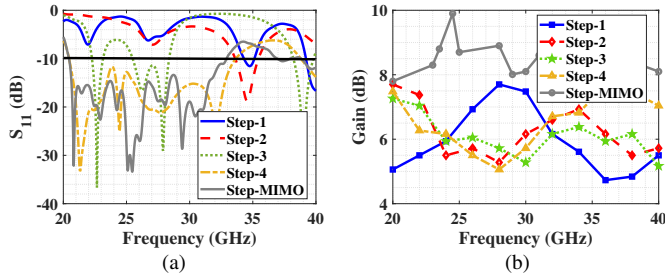


Fig. 4: Simulated results of all design steps (a) S-parameter and (b) gain.

This configuration improves impedance matching, as seen in Fig. 4(a). However, at this point, low gain and high mutual coupling are the primary issues, as seen in Figs. 3(b) and 3(c). An elliptical cross-shaped slot containing four CSRRs is etched in the ground plane, as shown in Fig. 3(e). As seen in Figs. 4(a) and 4(b), this step has improved the gain and port isolation. Although there is a minor decrease in impedance matching, this is tolerable for real-time applications.

To justify the selected ground-plane geometry, the CSRR and rotated rectangular slots act as sub-wavelength perturbations, introducing additional LC resonances that widen the impedance BW and slightly lower the effective resonant frequency, thereby contributing to miniaturization. At the same time, the cross-elliptical slots increase the local ground impedance and redirect surface currents away from adjacent feedlines, effectively suppressing mutual coupling and improving port isolation without requiring external superstrates. This combination of ground-plane loading and current steering enables a compact footprint while maintaining high realized gain and strong isolation suitable for closely spaced mm-wave MIMO elements.

D. Circuit model

The proposed slotted microstrip patch is analyzed using a parallel RLC equivalent circuit, providing physical insight

into its input behavior. Following standard patch-antenna modelling, the lumped-element values can be estimated in closed form [56], [57]. The equivalent capacitance is approximated by:

$$C = \frac{\epsilon_0 \epsilon_r a_e^2}{2h_t} \sec^2\left(\frac{\pi L_f}{a_e}\right) \quad (5)$$

where ϵ_0 is the permittivity of free space, ϵ_r is the substrate relative permittivity, a_e is the effective patch radius accounting for fringing fields, h_t is the substrate thickness, and L_f is the effective feed overlap.

The patch resistance and the inductance are approximated as $R \approx \frac{c\sqrt{\epsilon_r}}{4fh}$, and $L = \frac{1}{\omega^2 C}$, respectively [56], [57]. As a result, the value of the input impedance of the patch is:

$$Z_{patch} = \frac{1}{\frac{1}{R} + \frac{1}{j\omega L} + j\omega C} \quad (6)$$

where f as the operating frequency and $\omega = 2\pi f$. The slot loading introduces additional capacitance and inductance, estimated by [58]:

$$L_a = h \times \left[40.5 \left(\frac{a_e}{W_f} - 1 \right) - 75 \log \frac{a_e}{W_f} + 0.2 \times \left(\frac{a_e}{W_f} - 1 \right)^2 \right] \quad (7)$$

and

$$C_a = \sqrt{a_e W_f} \left[(10.1 \log \epsilon_r + 2.33) \frac{a_e}{W_f} - 12.6 \log \epsilon_r - 3.17 \right] \quad (8)$$

where W_f denotes the slot or feed width.

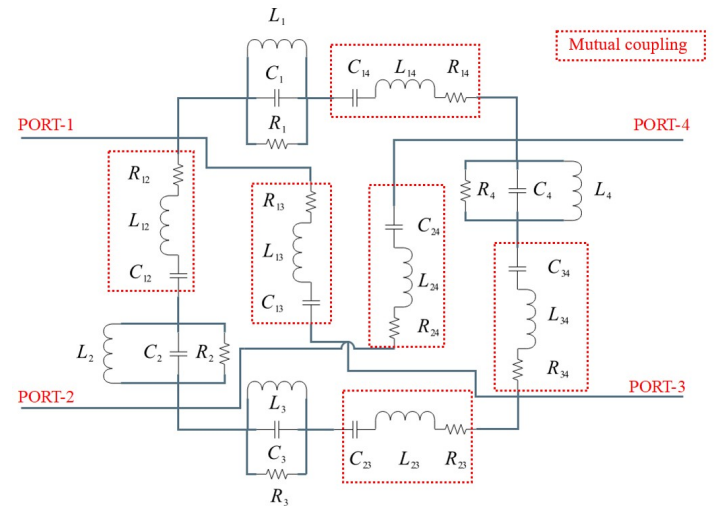


Fig. 5: Equivalent circuit of the final antenna: Lumped circuit model, $[R_1, R_2, R_3, R_4] = 8.926 \Omega$, $[C_1, C_2, C_3, C_4] = 1.237$ pF, and $[L_1, L_2, L_3, L_4] = 7.729$ pH.

A circular microstrip patch with a flower-shaped geometry is extended into a four-port (2×2) MIMO antenna by incorporating a CSRR, three parallel slots, and cross-elliptical slots in the ground plane. The CSRR is a key element for BW enhancement because it introduces an additional resonance and improving coupling. As the CSRR unit cell behaves as an LC resonator, its resonance frequency is given by [59]:

$$f_0 = \frac{1}{2\pi\sqrt{L_R C_R}} \quad (9)$$

where, L_R describes total inductance whereas C_R describes the total capacitance. Both can be explained as:

$$L_R = (4a_c - l)(2.303 \log(\frac{4l - g}{w_d})) \times 2 \times 10^{-4} \quad (10)$$

where a_c is the effective CSRR dimension, l is the side length of the CSRR ring, w_d is the trace width and g is the gap between CSRRs. Also, the capacitance is:

$$C_R = \frac{1}{2} [\frac{\epsilon_0 t}{g} + \frac{\sqrt{\epsilon_r}}{cZ_0} (4a_c - g)] \quad (11)$$

The terms Z_0 and c denote the characteristic impedance and the speed of light, respectively. These equivalent circuit formulations provide practical guidance for initial sizing and tuning of the antenna and its slots, and allow a physical interpretation of the input impedance and resonance behavior.

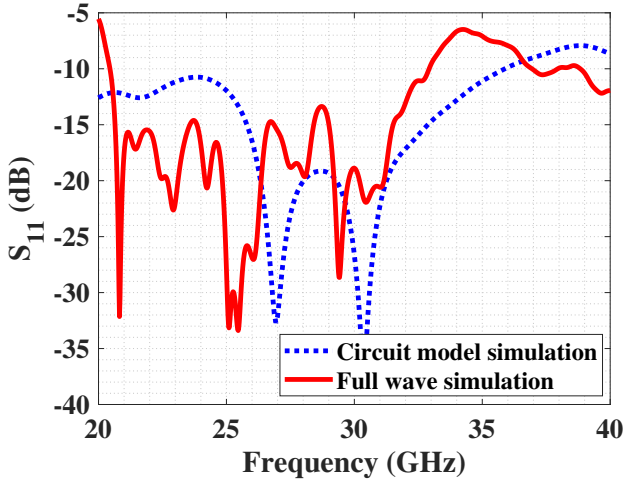


Fig. 6: Simulated reflection coefficient in CST and ADS.

III. PARAMETRIC STUDY

This section evaluates how key geometric parameters affect the antenna's operating frequency, BW, gain, and isolation. Insights from these sweeps are used to optimize the structure while preserving a compact footprint—the primary objective of the design. Only parameters shown to produce significant variations in impedance BW, realized gain, or inter-element isolation during preliminary sweeps are reported here; parameters with negligible influence are omitted for clarity.

A. Effect of the Patch Geometric Ratios

For the flower-shaped radiator, petal length is the primary tuning variable. Increasing it lowers the resonant frequency; decreasing it raises the resonance. The final petal length is selected to target the desired band, accounting for the number of petals and the overall radiator shape. In short, the careful choice of patch dimensions and their ratios determines the

operating frequency and BW without losing compactness. In the final design, adjusting the petal-length ratio (relative to the base circular patch) influences both the reflection coefficient $|S_{11}|$ and the achieved gain.

Varying the petal ratio in the final design patch affects both the reflection coefficient and the design gain.

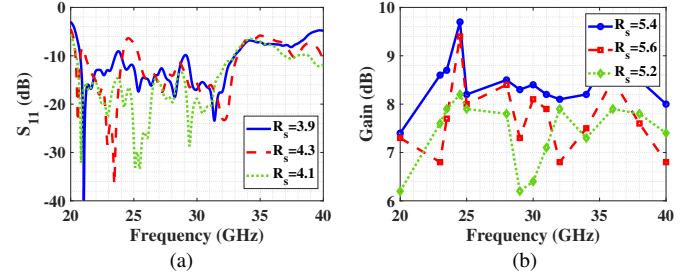


Fig. 7: Parametric analysis: impact of the R_s on the a) S_{11} and b) gain.

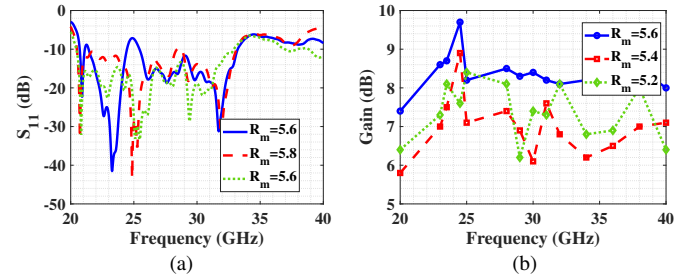


Fig. 8: Parametric analysis: impact of the R_m on the a) S_{11} and b) gain.

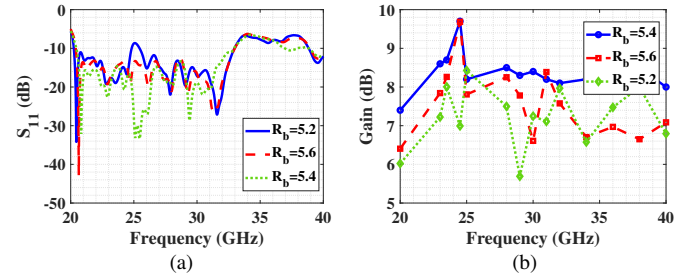


Fig. 9: Parametric analysis: impact of the R_b on the a) S_{11} and b) gain.

As illustrated in Fig. 7(a), Fig. 8(a), and Fig. 9(a), progressively changing the petal-length ratio in the proposed radiator reduces the operating BW. A similar trend appears in the realized gain (Fig. 7(b), Fig. 8(b), and Fig. 9(b)). Precise tuning is therefore critical. The best trade-off is obtained at $R_s = 4.1$ mm, $R_m = 5.4$ mm, and $R_b = 5.6$ mm, which delivers the maximum BW with strong impedance matching and the highest gain.

The proposed antenna enhances BW through controlled multi-resonant behavior. The petal-shaped radiator introduces additional current paths, generating closely spaced resonances. At the same time, the CSRR in the ground plane contributes

an LC resonance that couples with the fundamental patch mode. The rotated rectangular slots adjust the local ground impedance and flatten the input impedance slope, improving matching over a wider frequency span. By tuning the CSRR dimensions (C_a, C_b) and the slot geometry, the -10 dB BW can be increased or reduced, as confirmed by parametric sweeps.

B. Impact of Patch Slot Dimensions

Slots etched into the radiating patch significantly affect performance, particularly BW and impedance matching. Properly designed slots can broaden BW, tune the input impedance, and even enable miniaturization by lowering the resonant frequency. Fig. 10 illustrates how varying the cross-slot dimensions alters the BW: the slot width and length are the primary controls of the achievable BW. Precise tuning of these parameters is therefore essential to meet the target band while maintaining good matching.

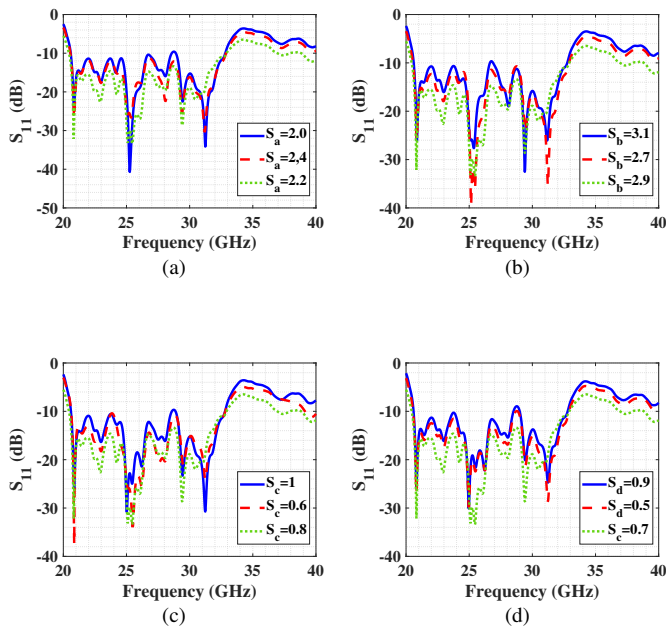


Fig. 10: Parametric analysis: impact of the dimension of the cross slots.

The final value of the dimension of the cross-slots for S_a , S_b , S_c , and S_d is 2.2 mm, 2.9 mm, 0.8 mm, and 0.9 mm, respectively.

C. Impact of CSRR Internal and External Ratios on Gain

Loading the radiator with a CSRR introduces an additional LC resonance that can miniaturize the antenna, shift its resonant frequencies, and modify radiation efficiency, often improving gain when properly tuned.

A parametric sweep of the CSRR geometry (inner and outer dimensions) in the final design confirms this sensitivity (Fig. 11). As the external CSRR ratio increases, the realized gain rises progressively up to ≈ 28 GHz; beyond 28 GHz, the gain gradually rolls off. The maximum gain of 9.8 dBi occurs at 24.5 GHz. To maintain acceptable gain across the

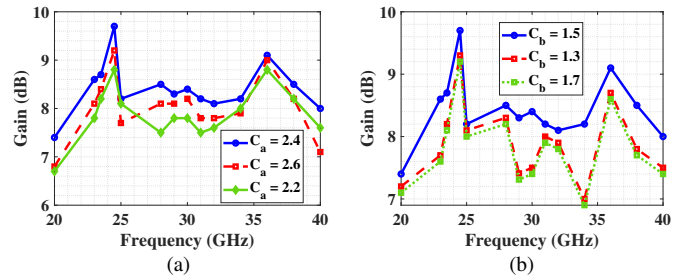


Fig. 11: Parametric analysis: impact of the CSRR ratios on gain, a) external ratio, b) internal ratio.

full operating band, the final design uses $C_a = 1.5$ mm (inner dimension) and $C_b = 2.4$ mm (outer dimension).

In the proposed antenna, the maximum realized gain is primarily governed by the electromagnetic loading introduced by the CSRR and the rotated rectangular slots in the ground plane. Adjusting the outer CSRR dimension (C_b) increases the effective magnetic coupling beneath the radiator, thereby enhancing forward radiation and reducing backward leakage, thereby improving peak gain to an optimal point. Similarly, modifying the orientation and length of the rotated slots redistributes surface currents, thereby reinforcing the broadside radiation pattern. On the radiating patch, the petal-length ratio affects the effective electrical aperture, enabling further gain enhancement when properly tuned. These parameters were jointly optimized to achieve the reported peak gain of 8.7-9.8 dBi without compromising BW or port isolation.

IV. SIMULATED AND MEASURED RESULTS

This section presents the simulated and measured performance of the proposed four-port MIMO antenna, including reflection coefficients, radiation patterns, realized gain, efficiency, and surface current distributions.

A. Experimental Setup

Design, optimization, and full-wave simulations were performed using CST Microwave Studio. The prototype was fabricated on Rogers RT/Duroid@5880, and mm-wave connectors were mounted on each feed line for measurement. Using a vector network analyzer (VNA), the S-parameters were measured. During each measurement, Port 1 was connected to the VNA while the remaining three ports were terminated with 50- Ω loads to ensure proper port conditions. Far-field patterns and realized gain were measured in an anechoic chamber: the antenna under test (AUT) was fixed on a rotary positioner placed in front of a standard-gain horn, enabling pattern acquisition over the required angular range. From the measured and simulated data, key MIMO figures, including the Envelope Correlation Coefficient (ECC), Mean Effective Gain (MEG), Channel Capacity Loss (CCL), and Diversity Gain (DG), were derived.

Photographs of the fabricated prototype (top and bottom views) are shown in Figs. 12(a) and 12(b); the S-parameter measurement setup is shown in Fig. 12(c). The far-field

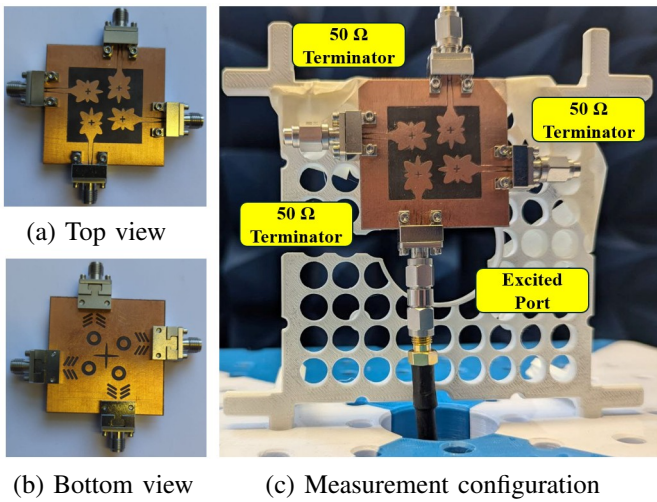


Fig. 12: Fabricated prototype: (a) top view, (b) bottom view, and (c) MIMO antenna VNA model for S-Parameter measurements.

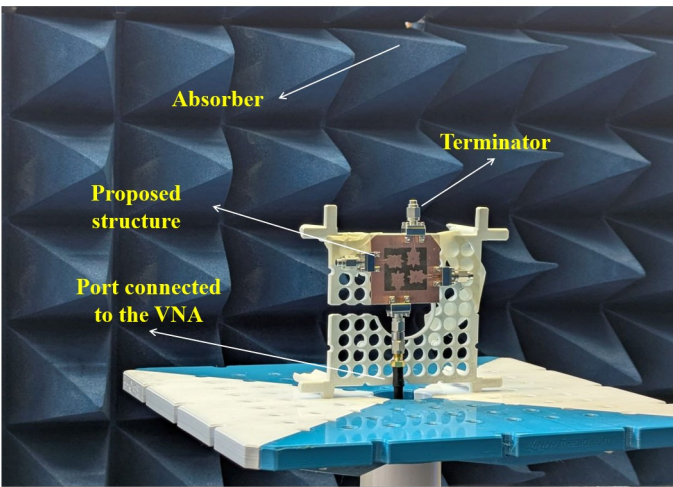


Fig. 13: Measurement of the proposed structure in an anechoic chamber.

measurement arrangement in the anechoic chamber is depicted in Fig. 13.

The measured gain and efficiency values obtained from these experimental characterizations are subsequently used as inputs to the deployment-oriented link-budget feasibility evaluation presented in Section VII.

B. Simulated and measured S-parameters

Figs. 14 and Fig. 15 compare the simulated and measured scattering parameters of the proposed array: Figs. 14 shows the reflection coefficient $|S_{11}|$, and Fig. 15 shows the transmission (coupling) coefficients $|S_{ij}|$ for $i \neq j$. Owing to the array's symmetry, results are reported for a representative port; the remaining ports exhibit the same behavior.

The measured and simulated $|S_{11}|$ confirm continuous coverage of the 5G NR n258 (24.25-27.50 GHz) and n257 (26.50-29.50 GHz) bands. Minor shifts in resonance frequency and matching depth are attributed to cable/connector losses

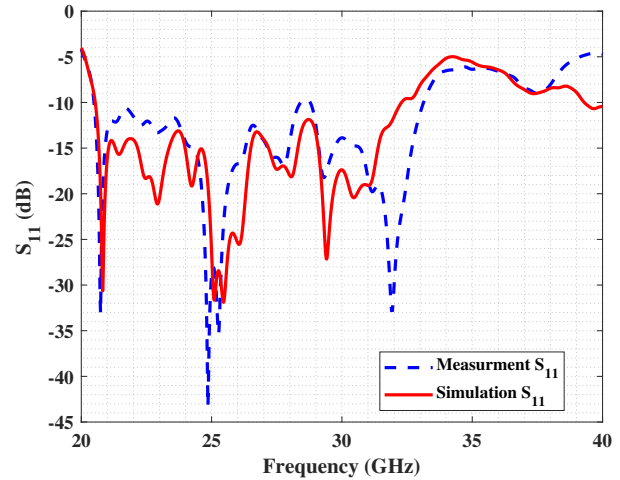


Fig. 14: Simulated and measured scattering parameters of the design: reflection coefficients.

and fabrication tolerances. For coupling, symmetry yields $|S_{12}| \approx |S_{13}| \approx |S_{14}|$ and $|S_{23}| \approx |S_{24}| \approx |S_{34}|$; accordingly, a single simulated trace is plotted for each equivalence set with the corresponding measured curve. The measured and simulated transmission coefficients show good agreement, with minor discrepancies due to ambient noise and manufacturing tolerances.

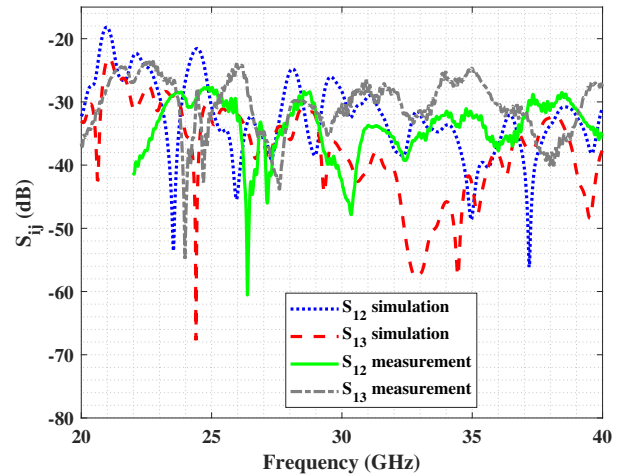


Fig. 15: Simulated and measured scattering parameters of the design: transmission coefficients.

There is acceptable agreement between the measured and simulated transmission coefficients. Ambient noise and fabrication intolerance are the cause of a small deviation.

The strong inter-port isolation in the proposed array results from the combination of orthogonal radiator orientations and evolved DGS, where CSRRs and rotated rectangular slots increase local ground impedance and interrupt surface-wave coupling between adjacent elements. The cross-elliptical slots further confine backward radiation and redirect surface currents, thereby contributing to additional isolation without the need for external superstrates. Increasing the strength or

density of these perturbations would compromise BW and gain, reflecting the inherent trade-off between isolation and overall radiation performance in compact mm-wave MIMO arrays.

C. Simulated and Measured Gain

Fig. 16 presents the realized gain over the full operating band for both simulation and measurement. The antenna maintains a high average gain of ≈ 8.7 dBi across the band, with peak gains of 9.8 dBi in n258 (24.25-27.50 GHz) and 8.8 dBi in n257 (26.50-29.50 GHz), suitable for a range of mm-wave applications. Overall, measured and simulated results agree well.

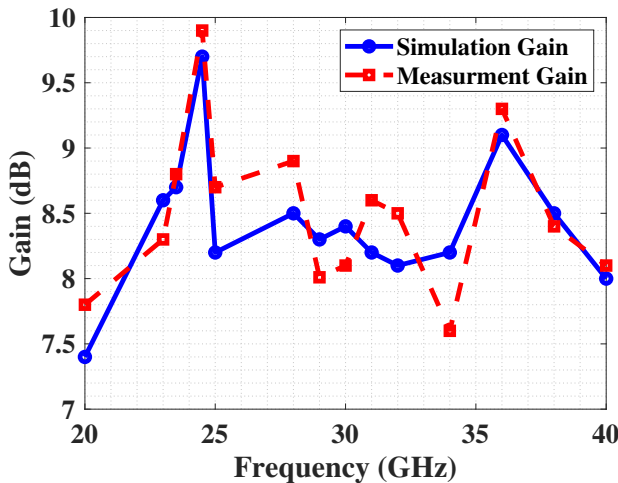


Fig. 16: Simulated and measured gain of the proposed MIMO structure.

Small discrepancies arise from several sources, including measurement noise and fabrication tolerances; frequency-dependent substrate losses and dispersion, which become more pronounced at higher mm-wave frequencies; and connector/cable effects (such as impedance mismatch and incomplete de-embedding). Given the broad BW, these effects are more pronounced near the band edges, where the measured gain can fall slightly below the simulated values.

D. Surface Current Distribution

Fig. 17 shows the surface-current density at 28 GHz for each port. For Port 1 (Fig. 17(a)), the current is concentrated along the feedline and across the radiator; Port 2 exhibits a similar pattern. Only a small current appears between Ports 1 and 2, indicating low mutual coupling. Ports 3 and 4 likewise concentrate current along their respective feeds and patches, with the weakest inter-element current observed between them consistent with very low coupling and high port isolation.

E. Farfield radiation pattern

A far-field pattern of the proposed design at 26, 27, 28, and 29 GHz is described in this section. The E-field (XY

plane) and H-field (YZ plane) are used to compute the far-field, respectively. The far-field patterns are measured at each of the four ports because the design features a variety of patterns. While measuring the distant field patterns, port 1 is stimulated, and the other ports are terminated using a 50Ω load (terminator).

The E-field and H-field patterns at mm-wave n258 (24.25-27.50 GHz) and n257 (26.59-29.50 GHz) for port 1 are shown in Figs. 13(a) to (e), respectively. At this frequency, the H-field is directed towards 0° , but the E-field exhibits a broad and focused direction to 30° . It is evident from the port 1 analysis that the primary E-field beam shifts direction, initially focusing at 30° and now at 315° , confirming its pattern-variety feature. Consequently, the design only offers pattern diversity in two dimensions. Similar predicted and measured radiation patterns are observed for each port, suggesting steady performance across the operational BW and near-uniform port alignment.

The measured and simulated patterns differ slightly, most likely due to ambient noise or cable losses that can affect antenna performance. However, the suggested MIMO array technology successfully captures the simulated and measured far-field radiation patterns, despite these minor differences, confirming its dependability.

Minor differences between measured and simulated patterns are attributed to ambient noise, cable/connector losses, and small alignment or fabrication tolerances, which are particularly pronounced at mm-wave frequencies due to the shorter wavelength and higher sensitivity of coaxial-to-PCB transitions. Despite these effects, the measured results closely track simulations, supporting the reliability of the proposed MIMO array.

V. MIMO ANTENNA PERFORMANCE

This section outlines key MIMO metrics, including diversity gain (DG), total active reflection coefficient (TARC), and envelope correlation coefficient (ECC), which are used to evaluate the proposed array.

A. Envelope correlation coefficient

ECC quantifies how similar two ports are in their radiated fields; lower values indicate weaker correlation and thus stronger diversity performance. By combining pattern diversity with reduced inter-element coupling in a single plane, the proposed layout achieves very low ECC and, consequently, high DG. Fig. 19 shows the isotropic ECC across the entire operating band, remaining below 0.002, which is indicative of excellent pattern diversity. The ECC for this broadband MIMO antenna is computed using the standard formulation in [60]:

$$\rho_e = \frac{A}{B + C} \quad (12)$$

where A, B, and C are:

$$A = \left| \int_0^{2\pi} \int_0^\pi XRP \cdot E_{\theta_1} \cdot E_{\theta_2}^* \cdot P_\theta + E_{\phi_1} \cdot E_{\phi_2}^* \cdot P_\phi d\Omega \right|^2 \quad (13)$$

$$B = \left| \int_0^{2\pi} \int_0^\pi XRP \cdot E_{\theta_1} \cdot E_{\theta_1}^* \cdot P_\theta + E_{\phi_1} \cdot E_{\phi_1}^* \cdot P_\phi d\Omega \right|^2 \quad (14)$$

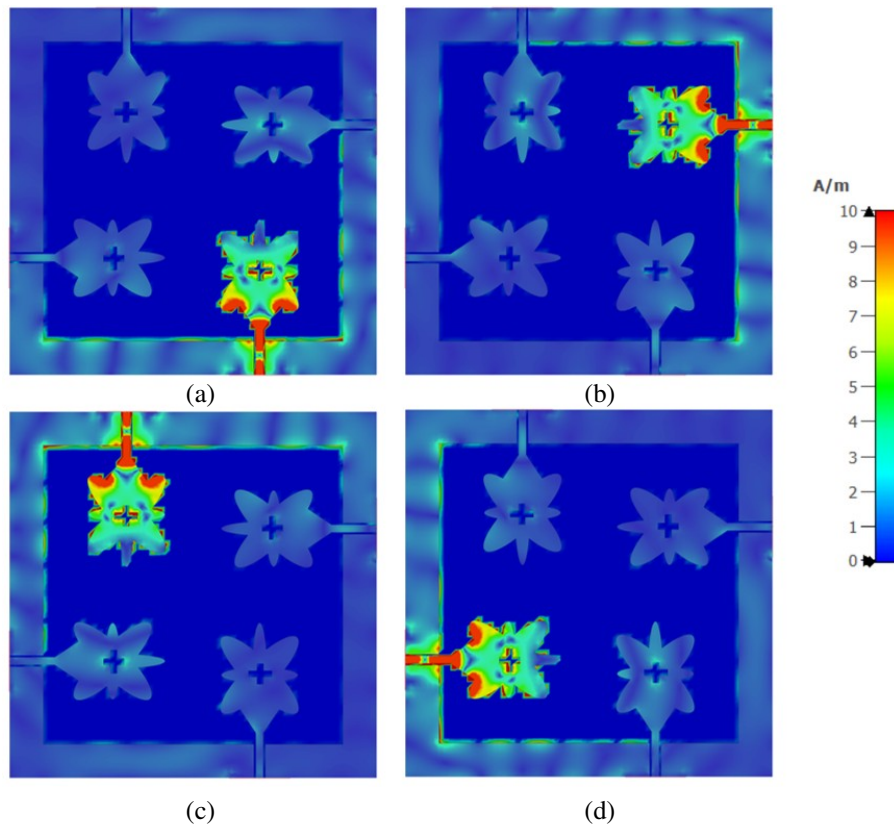


Fig. 17: Surface current distribution of the proposed design at 28 GHz: (a) Port 1, (b) Port 2, (c) Port 3, (d) Port 4.

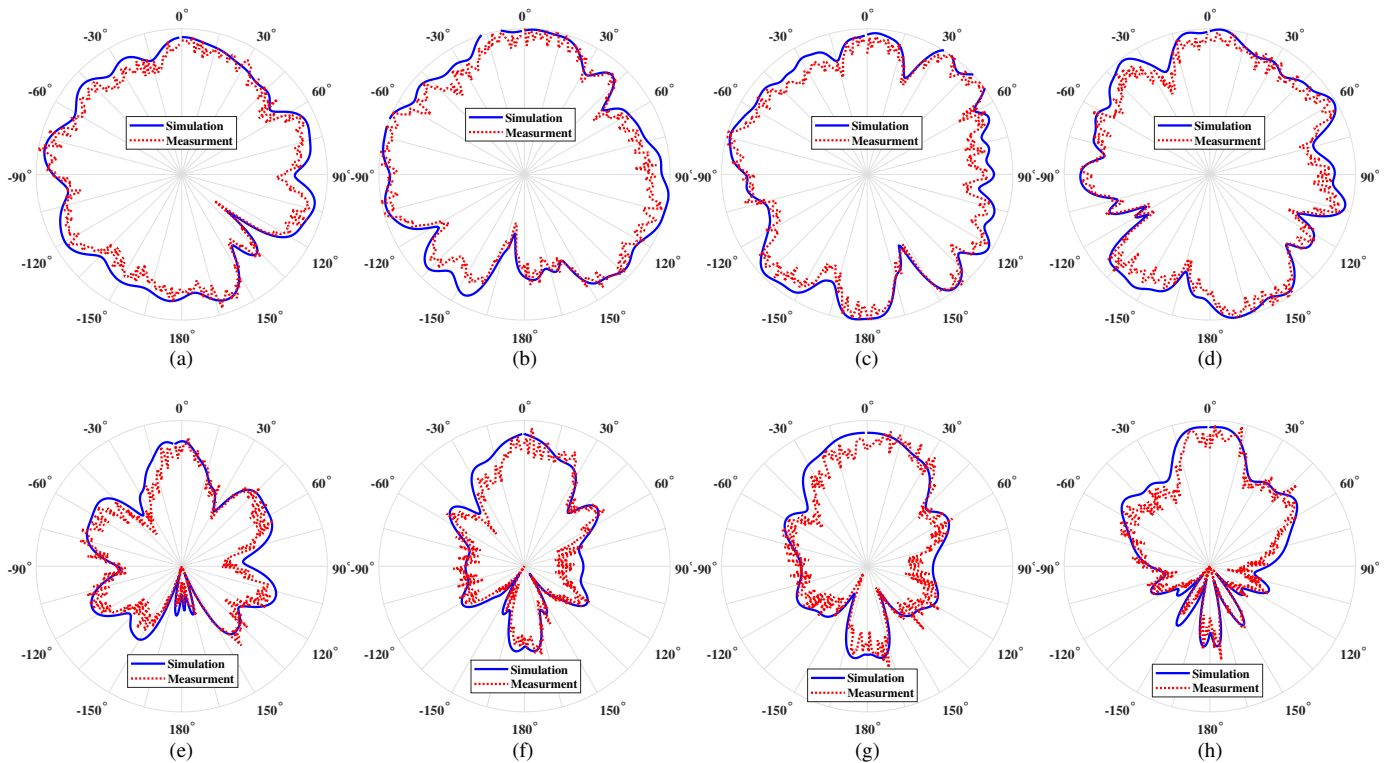


Fig. 18: Far-field radiation pattern at mm-wave n257 and n258 GHz: (a) 26 GHz, (b) 27 GHz, (c) 28 GHz and (d) 29 GHz shows E-field (XY-plane) patterns and (e) 26 GHz, (f) 27 GHz, (g) 28 GHz and (h) 29 GHz show H-field (XZ-plane) patterns respectively.

$$C = \left| \int_0^{2\pi} \int_0^\pi XRP \cdot E_{\theta_2} \cdot E_{\theta_2}^* \cdot P_\theta + E_{\phi_2} \cdot E_{\phi_2}^* \cdot P_\phi d\Omega \right|^2 \quad (15)$$

where ρ_e is envelope correlation coefficient, E_θ , E_ϕ are the far field radiation components, P_θ , P_ϕ are the angular power distribution, XRP is cross-polarization ratio and Ω is the solid angle

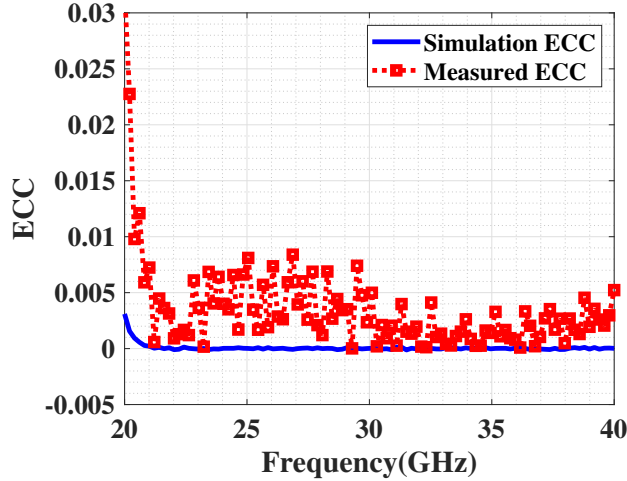


Fig. 19: MIMO simulated and measured ECC results.

B. Diversity gain analysis

Diversity gain (DG) quantifies the improvement in link reliability due to multiple uncorrelated radiation paths and is typically expressed in decibels. Once the ECC is known, DG is computed using the standard relation in Eq. (16), as given in [61], [62], which directly links DG to ECC. For the proposed array, the DG is ≈ 10 dB across the operating band. Measured values are slightly lower, attributable to normal fabrication tolerances.

$$DG = \sqrt{1 - ECC} \quad (16)$$

The measured and simulated diversity gains over the entire operating band are shown in Fig. 20.

C. The total active reflection coefficient (TARC)

The TARC curves evaluate impedance matching performance of a MIMO antenna under multiple ports excitation. Fig. 21 shows that the desired operating frequency band is less than -10 dB. An expression for computing TARC using the obtained S-parameters for a two-port network [62] is given by Eq. (17)

$$\Gamma = \frac{\sqrt{D + E}}{2} \quad (17)$$

where D and E are respectively:

$$D = |S_{11} + S_{12}e^{j\theta}| \quad (18)$$

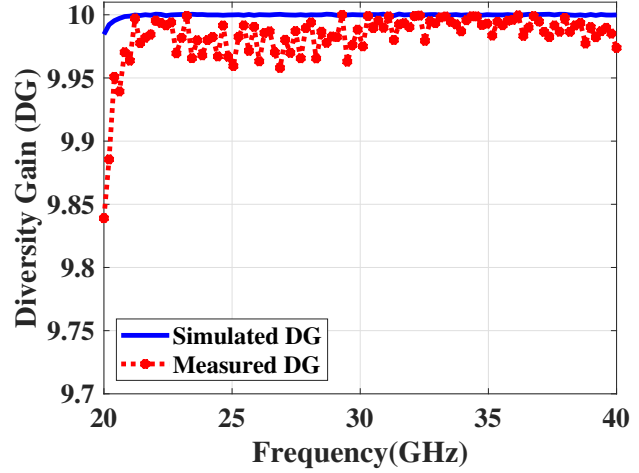


Fig. 20: MIMO simulated and measured DG results.

$$E = |S_{22} + S_{21}e^{j\theta}| |S_{33} + S_{31}e^{j\theta}| |S_{44} + S_{41}e^{j\theta}| \quad (19)$$

where Γ is the total active reflection coefficient, S_{ij} is the scattering parameters, and θ is the phase difference between input signals.

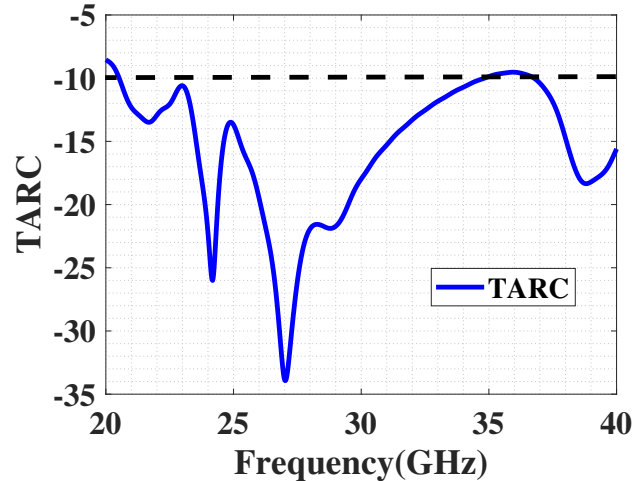


Fig. 21: MIMO simulated and measured TARC results.

VI. MIMO DIVERSITY ANALYSIS

This section provides a detailed discussion of the diversity parameters, including the mean effective gain, group-delay analysis, channel-capacity loss, and multiplexing efficiency.

A. Channel capacity loss (CCL)

The channel capacity loss of the proposed MIMO system demonstrates the quality of information transmission across the operational spectrum. A high data transfer rate is enabled by a low CCL value, which is highly desirable. Excellent data transmission is indicated by a CCL value of 0.5 bits/sec/Hz, while lossy and subpar data transfer is implied by values

more than 0.5 bits/sec/Hz. CCL is less than 0.4 bits/sec/Hz throughout the whole working band, as shown in Fig. 22. As a result, the recommended design has an excellent CCL across most of the operating range, indicating that it transmits data efficiently and with low loss.

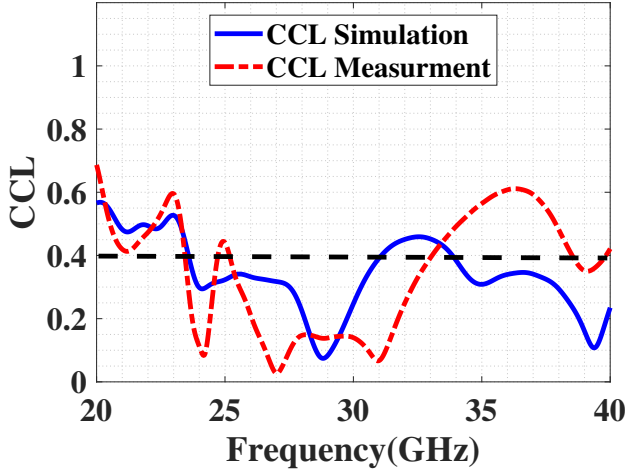


Fig. 22: MIMO simulated and measured CCL results.

The formulas shown below can be used to compute it [63].

$$CCL = -\log_2 \det(M) \quad (20)$$

where the value of the M is:

$$M = \begin{bmatrix} 1 - (|S_{ii}|^2 + |S_{ij}^2|) & -S_{ii} * S_{ij} - S_{ji} * S_{jj} \\ -S_{jj} * S_{ji} - S_{ij} * S_{ii} & 1 - (|S_{jj}|^2 + |S_{ji}^2|) \end{bmatrix} \quad (21)$$

B. Group delay analysis

Group delay quantifies the time shift experienced by the signal's envelope as it propagates through the device under test. In other words, it is the delay between the input and output amplitude envelopes, evaluated per frequency component; ideally, the envelope shape is preserved during the delay. Fig. 23 reports the group delay for the proposed MIMO array. We denote group delay (1,1) as the reflective path (Port 1 to Port 1), and group delay (1,2), (1,3), and (1,4) as the transmission paths from Port 1 to Ports 2, 3, and 4, respectively. Owing to the array's symmetry, (1,2) and (1,4) are essentially identical.

Minor envelope delays are observed below 25 GHz. The variation ranges from 31.2 GHz to 38.5 GHz, yet all traces remain within acceptable limits across the operational BW. Overall, the group delay of the proposed MIMO antenna is < 3.1 ns.

C. Mean effective gain (MEG)

The ability of an antenna to receive electromagnetic power in a multipath scenario is known as MEG. For appropriate diversity performance, the MEG under real-time conditions should be between -3 and -12. Thus, as illustrated in Fig. 24, the MEG values of every MIMO antenna in the suggested

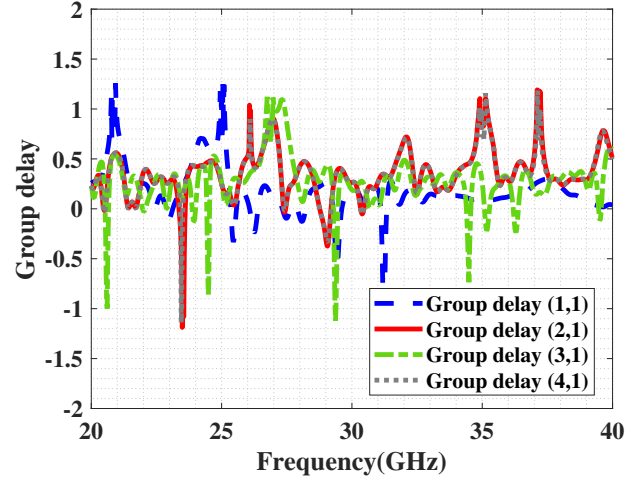


Fig. 23: MIMO simulated and measured group delay results.

architecture are verified. The value of the MEG with n number of antenna elements is calculated using Eq. (22) [64]:

$$MEG_i = \frac{1}{n} \left(1 - \sum_{j=1}^n |S_{ij}|^2 \right) \quad (22)$$

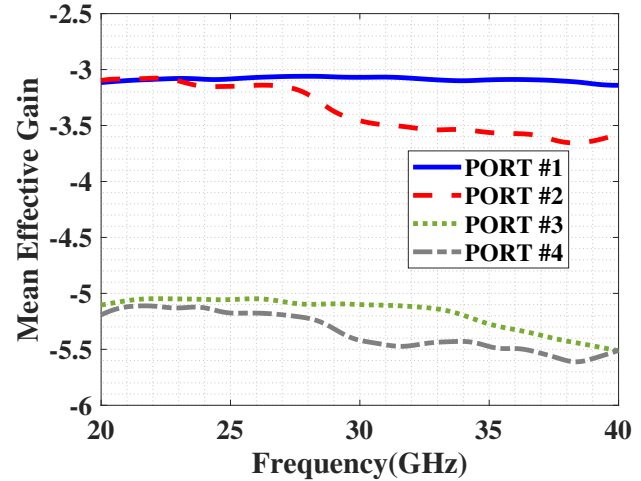


Fig. 24: Mean effective gain measurement of the proposed MIMO antenna.

D. Multiplexing efficiency

Multiplexing efficiency describes the power-efficiency losses or degradation incurred when using the tested MIMO antenna. Beyond the overall antenna efficiency, this crucial MIMO antenna system parameter is evaluated to reflect both port efficiencies and mutual correlation between antenna elements. The MIMO antenna's multiplexing efficiency (η_{mux}) is computed as:

$$\eta_{\text{mux}} = \frac{1}{n} \sum_{i=1}^n \eta_i \left(1 - \sum_{\substack{j=1 \\ j \neq i}}^n |\rho_{ij}|^2 \right) \quad (23)$$

Its functional form is shown in Fig. 25. In Eq. (23), n denotes the number of MIMO antenna ports, ρ_{ij} is the envelope correlation coefficient between ports i and j , and η_i represents the radiation efficiency of port i , including mismatch losses.

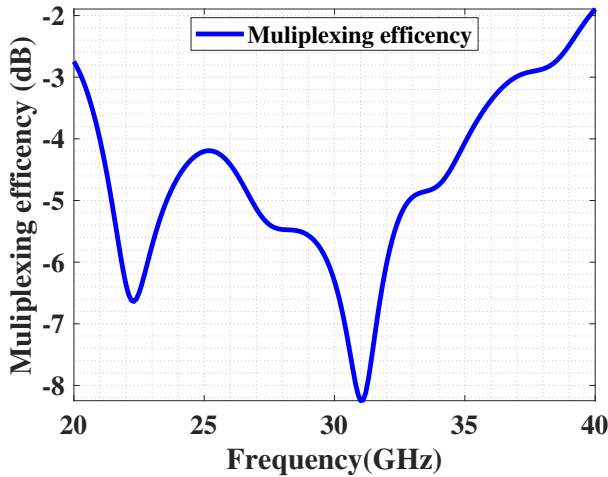


Fig. 25: Multiplexing calculation result of the proposed antenna

VII. LINK BUDGET ANALYSIS

Wideband mm-wave antennas are essential for high-data-rate wireless links because their broad impedance bandwidth enables support for wide communication channels. However, at 5G NR FR2 frequencies, propagation loss, blockage sensitivity, and multipath fading significantly influence achievable connectivity, particularly in compact IoT edge deployments operating under strict size and power constraints.

To translate the experimentally validated antenna performance into practical implications for IoT deployment, this section presents an analytical feasibility assessment of the link. The objective is to quantify achievable link margins using measured antenna parameters under realistic propagation assumptions, thereby connecting validated hardware performance to representative FR2 IoT edge scenarios. The proposed mm-wave MIMO antenna targets short- to medium-range deployments, including industrial sensor gateways, UAV-assisted monitoring platforms, and dense smart-factory connectivity operating in the 5G NR n257/n258 bands. In this analysis, the antenna gain and radiation efficiency are derived directly from measurements of the fabricated prototype, while the propagation component is modeled using a standard free-space/path-loss analytical framework. Consequently, the evaluation serves as a deployment-level feasibility benchmark grounded in experimentally validated front-end performance, providing practical insight into achievable coverage and link margin for mm-wave IoT edge connectivity.

As illustrated in Fig. 26, the transmitter (Tx) is fixed while the receiver (Rx) separation distance is varied. In the experimental setup, over-the-air transmission measurements were conducted from 0.2 m to 10 m due to practical laboratory constraints, including cable loss and the unavailability of longer, low-loss measurement cables at 28 GHz. This measured range enables validation of distance-dependent transmission behavior within near- to intermediate-field separations and provides experimentally grounded received-power data. For distances beyond 10 m, link performance is evaluated analytically using measured antenna gain and radiation efficiency, along with established free-space and PL models, extending the assessment to 80 m to reflect representative short- to medium-range FR2 IoT edge deployment scenarios. As shown in Fig. 27 (a)-(c), the measured link-margin results (up to 10 m) closely follow the corresponding simulated trends across different PL exponents ($n = 1.6, 2, \text{ and } 3$), confirming consistency between the fabricated prototype performance and the analytical propagation framework. This combined measured-analytical approach therefore provides both experimental validation at practical distances and deployment-level feasibility estimation at extended ranges.

An efficient and reliable wireless connection is confirmed when the link margin is greater than zero [51], [82]. The link margin indicates the difference between the power received and the power available at the receiver. Therefore, the power that Rx receives is calculated as follows:

$$P_{REC}(W) = kT + B_R + \frac{E_b}{N_0} \quad (24)$$

where k stands for the Boltzmann constant, $\frac{E_b}{N_0}$ is the energy-to-noise ratio for single-bit transmission, and T stands for Kelvin's temperature, which is assumed to be 290. B_R denotes the data transfer rate that the communication link can support while ensuring a minimal link margin, as indicated below:

$$LM(dB) = P_R - P_{REC} \quad (25)$$

The link budget is represented as:

$$P_t - FSPL + G_t + G_r + G_{MIMO} - L_{other} = P_r + Margin \quad (26)$$

where $FSPL$ stands for free space path loss (PL) and G_{MIMO} for MIMO antenna system gain. The rest of the losses that are not specifically taken into account are represented by L_{other} . In the considered IoT edge-node context, P_t corresponds to practical mm-wave transmit power levels of compact gateways or UAV-mounted platforms. At the same time, L_{other} captures typical RF-chain losses, connector effects, and system-level margin requirements. Testing becomes even more challenging in an NLOS scenario due to obstacles and reflections (L_{obs}). The budget for the NLOS link is as follows:

$$P_t - FSPL + G_t + G_r + G_{MIMO} - L_{other} - L_{obs} = P_r + Margin \quad (27)$$

At 28 GHz, link budgets are computed for several target bit rates. Here, $FSPL$ represents free-space PL; additional losses

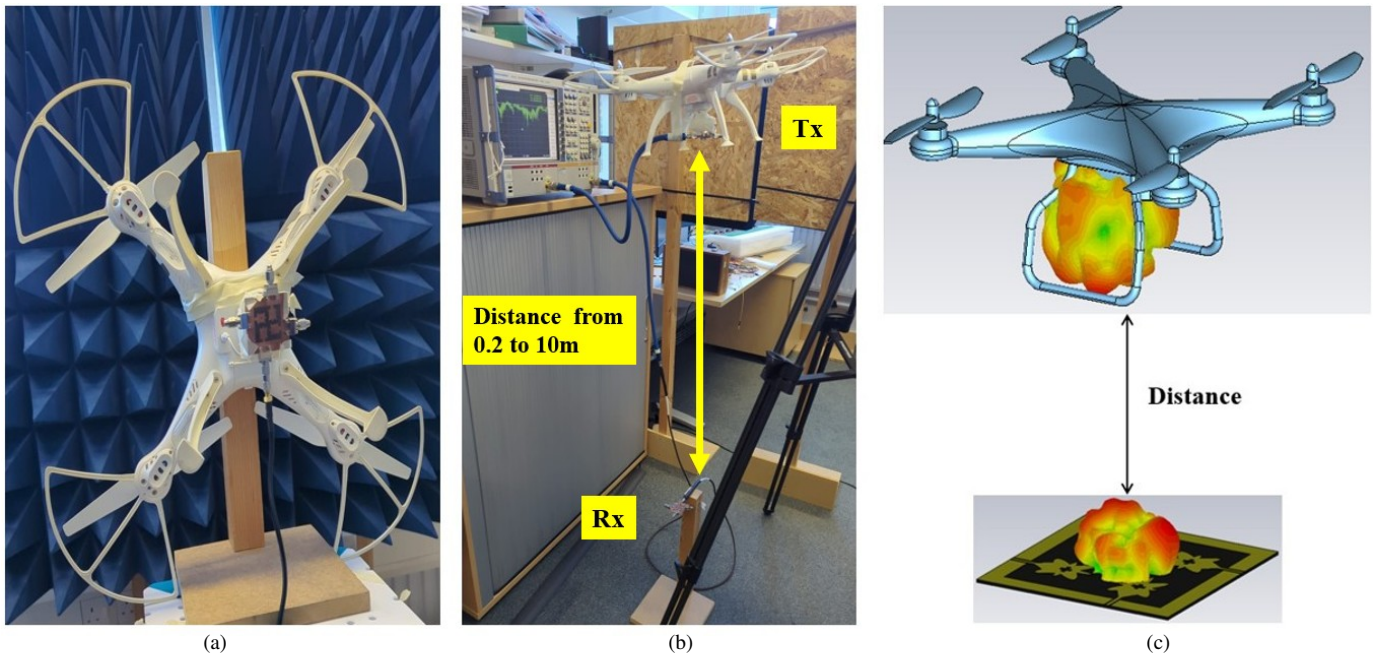


Fig. 26: MIMO prospective system a) position of the proposed MIMO antenna at the bottom of the drone, b) link budget measurement for VLOS system, c) link budget simulation.

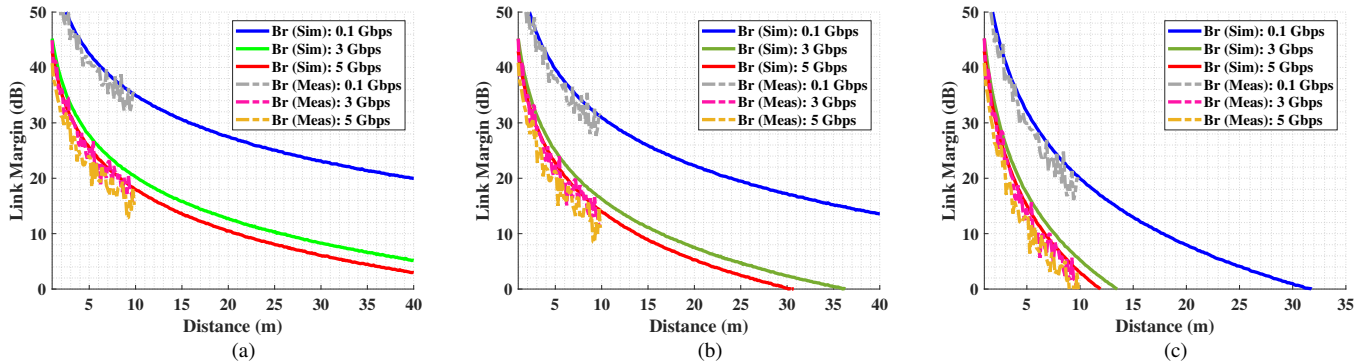


Fig. 27: Link budget simulation and measurement of proposed MIMO system (a) line of sight $n = 1.6$, (b) Free space $n = 2$, (c) NLOS $n = 3$.

due to obstructions or non-line-of-sight (NLOS) conditions are treated separately. LOS propagation with a PL exponent $n = 1.6$ is summarized in Fig. 27. Lowering the data rate increases the link margin. With a 20 dB link-margin target under LOS ($n = 1.6$), the coverage distance is:

- ≈ 60 m at 5 Gbps,
- > 80 m at 0.1 Gbps.

Free-space propagation with $n = 2$ (also in Fig. 27) yields:

- ≈ 20 m at 5 Gbps and 20 dB margin,
- > 35 m at 2 Gbps,
- > 80 m at 0.1 Gbps.

For NLOS conditions (higher effective loss), Fig. 27 indicates:

- reliable links up to ≈ 10 m at 5 Gbps,
- ≈ 15 m at 2 Gbps,
- and ≈ 30 m at 0.1 Gbps.

These results quantify the trade-off between data rate, environment, and coverage distance. Even when measured antenna

parameters are used, sufficient link margins are maintained for representative IoT edge deployment distances.

Fig. 28 illustrates the simulated and measured transmission coefficient (S_{21}) of the proposed MIMO antenna when it is mounted on a drone platform. The results are compared to the reference behavior of the antenna operating without the drone structure. As observed, the presence of the drone body introduces additional attenuation and frequency-dependent variations in the transmission response due to electromagnetic coupling, scattering, and structural blockage effects.

The measured S_{21} curve closely follows the simulated trend across the operating frequency band, confirming the validity of the numerical model. Slight discrepancies between simulation and measurement are mainly attributed to fabrication tolerances, measurement uncertainty, cable effects, and environmental reflections during the experimental setup. Notably, the reduction in transmission magnitude clearly indicates the drone platform's impact on antenna-to-antenna coupling, un-

TABLE II: State-of-the-art design comparison between the proposed antenna and other references.

Antenna structure	Number of Ports	Peak Gain (dBi)	Operational BW (GHz)	Isolation (dB)	Size ($\lambda_0 \times \lambda_0$)	Dielectric Substrate	Equivalent Circuit	Coverage Range
Ref. [28]	3	4.6	37.3-38.6	27.6	6.8×1.2	RT/Duroid@5880	-	-
Ref. [33]	2	5.2	36.9-37.0	21.0	3.2×1.7	RT/Duroid@5880	-	-
Ref. [65]	4	7.1	32	45.0	2.8×2.8	RT/Duroid@5880	-	-
Ref. [48]	4	8.6	28	26.0	4.2×4.2	RT/Duroid@5880	-	-
Ref. [66]	4	5.7	22-29	18.0	2.3×2.7	RT/Duroid@5880	-	-
Ref. [67]	4	6.6	26.0-40.0	18.1	1.5×2.1	RT/Duroid@5880	-	-
Ref. [68]	4	5.7	27.2-29.0	23.2	1.8×1.8	Rogers RO4003	-	-
Ref. [69]	4	7.7	27.7-28.4 / 37.6-38.1	20.0	1.6×0.8	Rogers 3003	Yes	60 m
Ref. [70]	4	8.1	27.5-29.3 / 37.0-38.2	22.0	2.6×2.2	Rogers RO4003	-	-
Ref. [71]	4	6.1	27.7-28.1 / 41.3-41.9	20.0	1.5×1.1	Rogers 3003	-	-
Ref. [72]	2	7.0	24-44	35.0	6.8×1.2	Rogers 4350	-	-
Ref. [73]	2	7.8	25-37	12.0	0.8×1.5	RT/Duroid@5880	-	-
Ref. [74]	2	8.4	24	30.0	1.2×1.6	Rogers 4350B	-	-
Ref. [75]	2	7.6	26-34	25.0	2.2×1.4	RT/Duroid@5880	-	-
Ref. [76]	4	6.5	38	45.0	4.2×6.1	RT/Duroid@5880	-	-
Ref. [77]	1	24	76-80	-	2.96×2.96	Lens Module	-	-
Ref. [78]	1	9.6	27.4-28.4	-	4.65×4.65	Rogers RO4350B	-	-
Ref. [79]	12	6.5	23-31	> 20	1.49×1.96	Rogers RO4350B	-	-
Ref. [80]	6	18	27-37	-	6.60×6.605	RogersRO4350B	-	-
Ref. [81]	4(array)	11.5	22-37 19-30	-	0.63×0.55	SIW horn cube	-	-
Proposed structure	4	9.8	26.5-29.5 / 24.3-27.5	25.0	3.8×3.8	RT/Duroid@5880	Yes	80 m

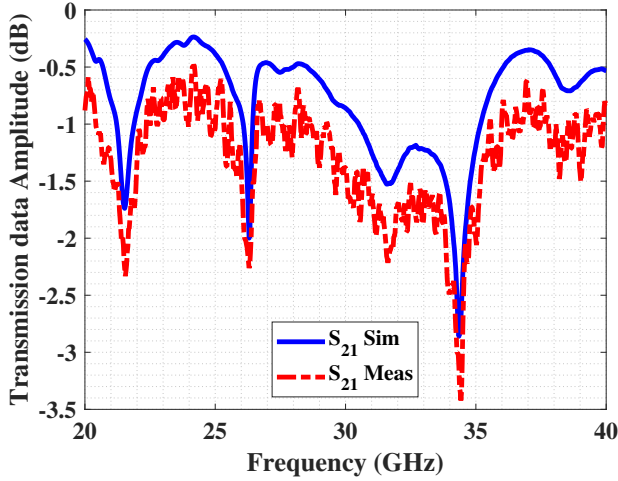


Fig. 28: Simulated and measured transmission data from drone to antenna.

underscoring the importance of accounting for realistic mounting conditions in practical airborne communication systems.

The observed degradation in transmission magnitude highlights the influence of the drone’s structure on the electromagnetic propagation path, thereby reducing the effective transmitted power between the antenna elements. Overall, this link-budget analysis complements the measured antenna characterization by explicitly translating validated gain, efficiency, and MIMO performance into achievable IoT deployment ranges. This hardware-grounded feasibility assessment is particularly important for FR2 IoT systems, where front-end performance directly determines link reliability and edge connectivity capability.

VIII. PATH LOSS ANALYSIS

Accurate path loss (PL) characterization is essential for evaluating the feasibility of mm-wave IoT deployments, since

FR2 propagation exhibits high free-space attenuation and strong sensitivity to environmental obstructions. To further substantiate the deployment oriented analysis presented in Section VII, this section evaluates large-scale PL behavior using established analytical and measurement-based models. Two commonly adopted modeling approaches are considered [83], [84]:

- The Close-In (CI) free-space reference distance model
- The Floating-Intercept (FI) model

The Close In path loss model is widely used in millimeter-wave channel characterization because it provides a physically meaningful reference based on the free space propagation loss at a close in distance. The CI model is expressed as [85]:

$$PL^{CI}(f, d)[dB] = FSPL(f, d_0) + 10n \log_{10}\left(\frac{d}{d_0}\right) + X_{\sigma}^{CI} \quad (28)$$

and the $FSPL(f, d_0)$ denotes the free space path loss at the reference distance d_0 , defined as:

$$FSPL(f, d_0) = 20 \log_{10}\left(\frac{4\pi d_0}{\lambda}\right) \quad (29)$$

In this formulation, n represents the path loss exponent describing the attenuation rate with distance, X_{σ}^{CI} is a zero mean Gaussian random variable representing log normal shadow fading with standard deviation σ in decibels (dB), λ is the carrier wavelength determined by the frequency, and d_0 denotes the reference distance, typically chosen as 1 m for millimeter-wave systems. To provide a flexible regression based fit to the measured data, the Floating Intercept model is also considered. The FI model expresses path loss as [86]:

$$PL^{FI}(d)[dB] = \alpha + 10\beta \log_{10}(d) + X_{\sigma}^{FI} \quad (30)$$

Here, α denotes the floating intercept in dB, β represents the slope of the distance dependent attenuation, and X_{σ}^{FI} is the shadow fading component.

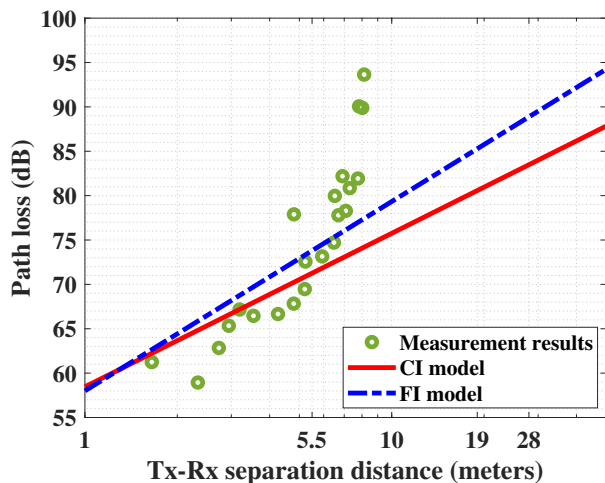


Fig. 29: Measured PL of the antenna mounted on the drone in LOS situation, simulated result by the FI and CI method at 28 GHz.

Measured path loss data for the drone-mounted antenna configuration are compared with both models (Fig. 29). The results demonstrate the expected logarithmic increase in attenuation with distance in LOS conditions at 28 GHz.

Both CI and FI models capture the measured trend. The FI model exhibits slightly closer agreement across the evaluated distance range due to its flexible parameterization, while the CI model retains stronger physical interpretability through its close-in reference anchor. This analysis confirms that the propagation assumptions used in the link budget evaluation are consistent with the measured large-scale attenuation behavior. Consequently, the deployment-oriented feasibility conclusions in Section VII are supported by realistic FR2 path loss characterization rather than idealized propagation assumptions.

IX. APPLICATION ENVIRONMENTS ANALYSIS AND DISCUSSION

The proposed antenna is designed for integration within compact FR2 IoT edge nodes, including industrial gateways and UAV-mounted sensing platforms. Its wide impedance bandwidth, low envelope correlation coefficient (ECC), and high port isolation support robust short-range connectivity in dense deployment environments subject to multipath and partial blockage. Rather than representing a standalone electromagnetic structure, the antenna is positioned as a communication front-end subsystem enabling reliable high-frequency IoT connectivity. In FR2 IoT deployments, achievable coverage, link stability, and spatial multiplexing capability are fundamentally constrained by antenna gain, radiation stability, and mutual coupling performance.

Table II presents a performance comparison with related mm-wave MIMO designs reported in the literature. The comparison focuses on electrical size, bandwidth, gain, port isolation, and system-level evaluation metrics. The objective of this comparison is technical benchmarking rather than venue-based positioning. Compared to several designs employing

multilayer superstrates or complex decoupling structures, the proposed architecture achieves wide n257/n258 coverage, high realized gain, and strong isolation using single-layer ground-plane engineering with evolved DGS and CSRR loading. This reduces fabrication complexity and thickness while maintaining performance suitable for compact IoT device integration. The combination of experimentally validated radiation performance, link-margin feasibility assessment, and large-scale path loss characterization collectively demonstrates the suitability of the proposed MIMO front-end for short- to medium-range FR2 IoT edge connectivity.

X. CONCLUSION

This work presents a compact 4×4 mm-wave MIMO antenna covering 5G NR n257 and n258 bands, targeting FR2 IoT edge and aerial connectivity scenarios. The proposed architecture integrates a T-shaped wideband radiator with CSRR-loaded and DGS-based ground-plane engineering to enhance impedance bandwidth, gain, and mutual coupling suppression without requiring multilayer superstrates or external decoupling networks. The fabricated prototype demonstrates strong agreement between simulated and measured results. The antenna achieves wideband FR2 coverage, measured peak gain of 9.8 dBi, low ECC (0.002), high diversity performance, low mutual coupling, and compact physical footprint ($3.86\lambda \times 3.86\lambda$). Beyond electromagnetic performance, the work includes a deployment-oriented link-budget analysis grounded in measured antenna parameters, along with a supporting large-scale path-loss evaluation. These analyses translate validated front-end performance into practical coverage and link-margin implications for short- to medium-range IoT edge deployments. The results demonstrate that the proposed mm-wave MIMO front-end provides a viable hardware solution for emerging 5G NR FR2 IoT connectivity, where the performance of the antenna subsystem directly governs achievable link reliability and integration feasibility.

ACKNOWLEDGMENT

Co-funded by the European Union. Views and opinions expressed are, however, those of the author(s) only and do not necessarily reflect those of the European Union or the European Research Executive Agency. Neither the European Union nor the granting authority can be held responsible for them. Besides that, this publication has emanated from research jointly funded by Taighde Éireann - Research Ireland under Grant number 13/RC/2094_2, the European Union's Marie Skłodowska-Curie Actions under Grant number 101126578, and the University of Galway.

REFERENCES

- [1] T. S. Rappaport, Y. Xing, G. R. MacCartney, A. F. Molisch, E. Mellios, and J. Zhang, "Overview of millimeter wave communications for fifth-generation (5g) wireless networks—with a focus on propagation models," *IEEE Transactions on antennas and propagation*, vol. 65, no. 12, pp. 6213–6230, 2017.
- [2] A. Mahmood, L. Beltramelli, S. F. Abedin, S. Zeb, N. I. Mowla, S. A. Hassan, E. Sisinni, and M. Gidlund, "Industrial iot in 5g-and-beyond networks: Vision, architecture, and design trends," *IEEE Transactions on Industrial Informatics*, vol. 18, no. 6, pp. 4122–4137, 2021.

- [3] H. Zakeri, P. Khoddami, G. Moradi, M. Alibakhshikenari, R. Abd-Elhameed, S. Koziel, and M. Dalarsson, "Path loss model estimation at indoor offices environment by using deep neural network and catboost for millimeter wave 5g wireless application," *IEEE Access*, 2024.
- [4] M. Abuyaghi, S. Si-Mohammed, G. Shaker, and C. Rosenberg, "Positioning in 5g networks: Emerging techniques, use cases, and challenges," *IEEE Internet of Things Journal*, 2024.
- [5] J. S. Seyyedi, R. S. Shirazi, and G. Moradi, "A dual-band lpda antenna based on mxene for high-band 5g application," in *2024 32nd International Conference on Electrical Engineering (ICEE)*. IEEE, 2024, pp. 1–4.
- [6] X. Wang, T. Li, X. Xiong, Y. Gao, and Z. Ning, "Federation chain for data privacy protection in industrial internet of things: The perspective from 5g core networks," *IEEE Internet of Things Journal*, 2024.
- [7] H. Zakeri, R. S. Shirazi, and G. Moradi, "An accurate model to estimate 5g propagation path loss for the indoor environment," *arXiv preprint arXiv:2302.10057*, 2023.
- [8] F. Arshad, A. Ahmad, Y. Amin, M. A. B. Abbasi, and D.-Y. Choi, "Mimo antenna array with the capability of dual polarization reconfiguration for 5g mm-wave communication," *Scientific reports*, vol. 12, no. 1, p. 18298, 2022.
- [9] S. Nej, A. Ghosh, S. Ahmad, J. Kumar, A. Ghaffar, and M. I. Hussein, "Design and characterization of 10-elements mimo antenna with improved isolation and radiation characteristics for mm-wave 5g applications," *IEEE Access*, vol. 10, pp. 125 086–125 101, 2022.
- [10] J. S. Yalli, M. H. Hasan, and A. Badawi, "Internet of things (iot): Origin, embedded technologies, smart applications and its growth in the last decade," *IEEE access*, 2024.
- [11] T. Raj, R. Mishra, P. Kumar, and A. Kapoor, "Advances in mimo antenna design for 5g: A comprehensive review," *Sensors*, vol. 23, no. 14, p. 6329, 2023.
- [12] N. Kishore and A. Senapati, "5g smart antenna for iot application: A review," *International Journal of Communication Systems*, vol. 35, no. 13, p. e5241, 2022.
- [13] E.-Z. G. Bozis, N. C. Sagias, M. C. Batistatos, M.-A. Kourtis, G. K. Xilouris, and A. Kourtis, "Enhancing 5g performance: A standalone system platform with customizable features," *AEU-International Journal of Electronics and Communications*, vol. 187, p. 155515, 2024.
- [14] X. Xia, F. Wu, C. Yu, Z. Jiang, J. Xu, S.-Y. Tang, Z. Wang, Y. Yao, and W. Hong, "Millimeter-wave and sub-6-ghz aperture-shared antenna and array for mobile terminals accessing 5g/6g-enabled iot scenarios," *IEEE Internet of Things Journal*, vol. 11, no. 10, pp. 18 808–18 823, 2024.
- [15] S. A. Khorasani, H. Zakeri, G. Moradi, M. Alibakhshikenari, C. H. See, and E. Limiti, "Orbital angular momentum with the approach of using in sub-6ghz 5g mobile communications for wireless applications," in *2024 6th Global Power, Energy and Communication Conference (GPECOM)*. IEEE, 2024, pp. 1–4.
- [16] J. Hao, N. Yan, Y. Luo, H. Fu, and K. Ma, "A low-cost dual-band multimode high-gain stacked-patch antenna based on sisl for 5g applications," *IEEE Antennas and Wireless Propagation Letters*, vol. 21, no. 1, pp. 4–8, 2021.
- [17] M. U. Khan, A. Muhammad, M. S. Sharawi, M. Alathbah, *et al.*, "Singly-fed large frequency ratio composite dielectric resonator antenna for sub-6 ghz and mm-wave 5g applications," *IEEE access*, 2024.
- [18] J.-J. Lo, Z. N. Chen, *et al.*, "Design of a broadband millimeter-wave array antenna for 5g applications," *IEEE Antennas and Wireless Propagation Letters*, vol. 22, no. 5, pp. 1030–1034, 2022.
- [19] J. Khan, S. Ullah, U. Ali, F. A. Tahir, I. Peter, and L. Matekovits, "Design of a millimeter-wave mimo antenna array for 5g communication terminals," *Sensors*, vol. 22, no. 7, p. 2768, 2022.
- [20] M. Parvaneh, H. Zakeri, G. Moradi, M. Alibakhshikenari, B. Alshammari, C. H. See, B. Virdee, S. K. Podilchak, and E. Limiti, "A feasibility study to practically implement a high-performance circularly polarised antenna array for point-to-point wireless communication," *IET Microwaves, Antennas & Propagation*, vol. 20, no. 1, p. e70078, 2026.
- [21] F. A. P. de Figueiredo, "An overview of massive mimo for 5g and 6g," *IEEE Latin America Transactions*, vol. 20, no. 6, pp. 931–940, 2022.
- [22] S. Khan, O. Khan, S. A. A. Shah, J. Nasir, B. T. Malik, S. Khan, and S. Koziel, "Highly-compact wideband high-gain four-element mimo antenna for 5g new radio iot," *IEEE Internet of Things Journal*, 2025.
- [23] N.-E. Mehenni, C. Zebiri, Y. Tighilt, A. Rivadeneyra, M. Alibakhshikenari, T. Saber, I. Elfergani, K. Karaçuğa, J. Rodriguez, P. Livreri, *et al.*, "Miniaturized low-interference cpw-fed mimo antenna on jeans textile for wearable biomedical applications in the 5.8 ghz ism band," in *2025 30th Asia-Pacific Conference on Communications (APCC)*. IEEE, 2025, pp. 1–6.
- [24] H. Zakeri, M. Veysi, G. Moradi, M. Alibakhshikenari, P. Liveri, T. A. Denidni, S. M. Koziel, I. Dayoub, and E. Limiti, "A compact dual circularly polarized mimo antenna with controlled slots for 5g wireless applications across mm-wave spectrum," in *2024 17th United Conference on Millimetre Waves and Terahertz Technologies (UCMMT)*. IEEE, 2024, pp. 194–198.
- [25] Y.-H. Yang, B.-H. Sun, and J.-L. Guo, "A low-cost, single-layer, dual circularly polarized antenna for millimeter-wave applications," *IEEE Antennas and Wireless Propagation Letters*, vol. 18, no. 4, pp. 651–655, 2019.
- [26] I. Khan, C. Song, H. Ullah, X. Qi, K. Zhang, M. M. Kamalf, Y. Shao, T. Gong, S. Khan, P. Livreri, *et al.*, "A novel multiband low mutual coupling quad-element mimo antenna for advanced communication systems," *IEEE Access*, 2025.
- [27] H. Bendjedi, S. Mekki, C. Zebiri, I. Elfergani, M. Alibakhshikenari, T. Saber, A. Rivadeneyra, J. Rodriguez, P. Livreri, and H. Zakeri, "High-isolation siw-based mimo antenna for mid x-band wireless applications," in *2025 30th Asia-Pacific Conference on Communications (APCC)*. IEEE, 2025, pp. 1–5.
- [28] E. Al Abbas, M. Ikram, A. T. Mobashsher, and A. Abbosh, "Mimo antenna system for multi-band millimeter-wave 5g and wideband 4g mobile communications," *IEEE Access*, vol. 7, pp. 181 916–181 923, 2019.
- [29] H. Zakeri, R. Azizpour, P. Khoddami, G. Moradi, M. Alibakhshikenari, C. H. See, T. A. Denidni, F. Falcone, S. Koziel, and E. Limiti, "Low-cost multiband four-port phased array antenna for sub-6 ghz 5g applications with enhanced gain methodology in radio-over-fiber systems using modulation instability," *IEEE Access*, 2024.
- [30] H. Marzouk, M. Ahmed, and A. Shaalan, "A novel dual-band 28/38 ghz afsl mimo antenna for 5g smartphone applications," in *Journal of Physics: Conference Series*, vol. 1447, no. 1. IOP Publishing, 2020, p. 012025.
- [31] D. T. T. Tu, N. G. Thang, N. T. Ngoc, N. T. B. Phuong, and V. Van Yem, "28/38 ghz dual-band mimo antenna with low mutual coupling using novel round patch ebg cell for 5g applications," in *2017 International Conference on Advanced Technologies for Communications (ATC)*. IEEE, 2017, pp. 64–69.
- [32] P. M. Sunthari and R. Veeramani, "Multiband microstrip patch antenna for 5g wireless applications using mimo techniques," in *2017 First international conference on recent advances in aerospace engineering (ICRAAE)*. IEEE, 2017, pp. 1–5.
- [33] M. N. Hasan, S. Bashir, and S. Chu, "Dual band omnidirectional millimeter wave antenna for 5g communications," *Journal of Electromagnetic Waves and Applications*, vol. 33, no. 12, pp. 1581–1590, 2019.
- [34] M. Khalid, S. Iffat Naqvi, N. Hussain, M. Rahman, Fawad, S. S. Mirjavadi, M. J. Khan, and Y. Amin, "4-port mimo antenna with defected ground structure for 5g millimeter wave applications," *Electronics*, vol. 9, no. 1, p. 71, 2020.
- [35] S. B. Paiva, A. G. D. Junior, V. P. S. Neto, and A. G. D'Assunção, "A new compact dual-polarized mimo antenna using slot and parasitic element decoupling for 5g and wlan applications," *Electronics*, vol. 11, no. 13, p. 1943, 2022.
- [36] C. Murat, M. Alibakhshikenari, P. Parand, H. Zakeri, R. Afrozeh, B. Virdee, L. Kohalvandi, P. Longhi, and E. Limiti, "Millimeter-wave antenna design inspired by half-ring resonators for 5g communication systems," in *2024 2nd International Conference on Information Network and Computer Communications (INCC)*. IEEE, 2024, pp. 59–64.
- [37] N. Hussain, M.-J. Jeong, J. Park, and N. Kim, "A broadband circularly polarized fabry-perot resonant antenna using a single-layered prs for 5g mimo applications," *IEEE Access*, vol. 7, pp. 42 897–42 907, 2019.
- [38] A. A. Khan, S. A. Naqvi, M. S. Khan, and B. Ijaz, "Quad port miniaturized mimo antenna for uwb 11 ghz and 13 ghz frequency bands," *AEU-International Journal of Electronics and Communications*, vol. 131, p. 153618, 2021.
- [39] M. M. Hasan, M. T. Islam, M. Samsuzzaman, M. H. Baharuddin, M. S. Soliman, A. Alzamil, I. I. Abu Sulayman, and M. S. Islam, "Gain and isolation enhancement of a wideband mimo antenna using metasurface for 5g sub-6 ghz communication systems," *Scientific reports*, vol. 12, no. 1, p. 9433, 2022.
- [40] M. A. Abbas, A. Allam, A. Gaafar, H. M. Elhennawy, and M. F. A. Sree, "Compact uwb mimo antenna for 5g millimeter-wave applications," *Sensors*, vol. 23, no. 5, p. 2702, 2023.
- [41] M. E. Munir, S. H. Kiani, H. S. Savci, M. Marey, J. Khan, H. Mostafa, and N. O. Parchin, "A four element mm-wave mimo antenna system with wide-band and high isolation characteristics for 5g applications," *Micromachines*, vol. 14, no. 4, p. 776, 2023.

- [42] J. Zhang, C. Du, and R. Wang, "Design of a four-port flexible uwb-mimo antenna with high isolation for wearable and iot applications," *Micromachines*, vol. 13, no. 12, p. 2141, 2022.
- [43] M. A. Khan, A. G. Al Harbi, S. H. Kiani, A. N. Nordin, M. E. Munir, S. I. Saeed, J. Iqbal, E. M. Ali, M. Alibakhshikenari, and M. Dalarsson, "mmwave four-element mimo antenna for future 5g systems," *Applied Sciences*, vol. 12, no. 9, p. 4280, 2022.
- [44] A. Desai, J. Kulkarni, M. Kamruzzaman, Š. Hubálovský, H.-T. Hsu, and A. A. Ibrahim, "Interconnected cpw fed flexible 4-port mimo antenna for uwb, x, and ku band applications," *IEEE Access*, vol. 10, pp. 57 641–57 654, 2022.
- [45] Y.-F. Tsao, A. Desai, and H.-T. Hsu, "Dual-band and dual-polarization cpw fed mimo antenna for fifth-generation mobile communications technology at 28 and 38 ghz," *IEEE Access*, vol. 10, pp. 46 853–46 863, 2022.
- [46] A. Desai, M. Palandoken, J. Kulkarni, G. Byun, and T. K. Nguyen, "Wideband flexible/transparent connected-ground mimo antennas for sub-6 ghz 5g and wlan applications," *IEEE Access*, vol. 9, pp. 147 003–147 015, 2021.
- [47] S. Tariq, S. I. Naqvi, N. Hussain, and Y. Amin, "A metasurface-based mimo antenna for 5g millimeter-wave applications," *IEEE Access*, vol. 9, pp. 51 805–51 817, 2021.
- [48] I. Ud Din, M. Alibakhshikenari, B. S. Virdee, R. K. R. Jayanthi, S. Ullah, S. Khan, C. H. See, L. Golunski, and S. Koziel, "Frequency-selective surface-based mimo antenna array for 5g millimeter-wave applications," *Sensors*, vol. 23, no. 15, p. 7009, 2023.
- [49] S. Tariq, Q. Hussain, M. S. Alzaidi, R. M. Ghoniem, M. Alibakhshikenari, A. A. Althwayb, B. S. Virdee, and M. Aslam, "Frequency selective surfaces-based miniaturized wideband high-gain monopole antenna for uwb systems," *AEU-International Journal of Electronics and Communications*, vol. 170, p. 154841, 2023.
- [50] P. P. Shome, T. Khan, A. A. Kishk, and Y. M. Antar, "Quad-element mimo antenna system using half-cut miniaturized uwb antenna for iot-based smart home digital entertainment network," *IEEE Internet of Things Journal*, vol. 10, no. 20, pp. 17 964–17 976, 2023.
- [51] A. Desai, H.-T. Hsu, B. M. Yousef, A. M. Ameen, Y.-F. Tsao, and A. A. Ibrahim, "Uwb connected ground transparent 4-port flexible mimo antenna for iot applications," *IEEE Internet of Things Journal*, vol. 11, no. 7, pp. 12 475–12 484, 2023.
- [52] H. Zakeri, M. Parvaneh, and G. Moradi, "A compact rhcp and lhcp truncated corner patch series-fed array antenna," *International Journal of Electronics Letters*, vol. 11, no. 1, pp. 125–133, 2023.
- [53] N. Alsaab, K. Alhassoon, F. Alsaleem, F. N. Alsunaydih, S. O. Madbouly, S. A. Khaleel, A. M. Ameen, and M. Shaban, "High-performance series-fed array multiple-input multiple-output antenna for millimeter-wave 5g networks," *Sensors*, vol. 25, no. 4, p. 1036, 2025.
- [54] Y. Zhu, K. Chen, S.-Y. Tang, C. Yu, and W. Hong, "Ultrawideband strip-loaded slotted circular patch antenna array for millimeter-wave applications," *IEEE Antennas and Wireless Propagation Letters*, vol. 22, no. 9, pp. 2230–2234, 2023.
- [55] H. Li, J. Du, X.-X. Yang, and S. Gao, "Low-profile all-textile multiband microstrip circular patch antenna for wlan applications," *IEEE Antennas and Wireless Propagation Letters*, vol. 21, no. 4, pp. 779–783, 2022.
- [56] Z.-Y. Zhang, C. F. Ding, Y. Zeng, F.-C. Chen, Y. Li, Q.-X. Chu, and M. Yu, "Circuit model for nth-order stacked patch antenna, parameter extraction, and radiation prediction," *IEEE Transactions on Antennas and Propagation*, vol. 72, no. 2, pp. 1329–1342, 2023.
- [57] D. Samantaray, S. K. Ghosh, and S. Bhattacharyya, "Modified slotted patch antenna with metasurface as superstrate for dual-band applications," *IEEE Antennas and Wireless Propagation Letters*, vol. 22, no. 1, pp. 109–113, 2022.
- [58] O. Sokunbi, H. Attia, A. Hamza, A. Shamim, Y. Yu, and A. A. Kishk, "New self-isolated wideband mimo antenna system for 5g mm-wave applications using slot characteristics," *IEEE Open Journal of Antennas and Propagation*, vol. 4, pp. 81–90, 2023.
- [59] H. Sarfraz, S. Khan, N. Khan, N. Gohar, S. A. A. Shah, J. Nasir, and M. Dalarsson, "Next-generation multiband wireless systems: A compact cssr-based mimo dielectric resonator antenna approach," *IEEE Access*, vol. 12, pp. 4910–4924, 2023.
- [60] A. K. Singh and S. Pal, "Compact self-isolated extremely low ecc folded-siw-based slot mimo antenna for 5g application," *IEEE Antennas and Wireless Propagation Letters*, vol. 23, no. 1, pp. 194–198, 2023.
- [61] W. M. Abdulkawi, W. A. Malik, S. U. Rehman, A. Aziz, A. F. A. Sheta, and M. A. Alkanhal, "Design of a compact dual-band mimo antenna system with high-diversity gain performance in both frequency bands," *Micromachines*, vol. 12, no. 4, p. 383, 2021.
- [62] A. Ahmad, D.-y. Choi, and S. Ullah, "A compact two elements mimo antenna for 5g communication," *Scientific Reports*, vol. 12, no. 1, p. 3608, 2022.
- [63] A. Khan, S. Bashir, S. Ghafoor, and K. K. Qureshi, "Mutual coupling reduction using ground stub and ebg in a compact wideband mimo-antenna," *IEEE access*, vol. 9, pp. 40 972–40 979, 2021.
- [64] D. Serghiou, M. Khalily, V. Singh, A. Araghi, and R. Tafazolli, "Sub-6 ghz dual-band 8 × 8 mimo antenna for 5g smartphones," *IEEE Antennas and Wireless Propagation Letters*, vol. 19, no. 9, pp. 1546–1550, 2020.
- [65] M. Hussain, E. Mousa Ali, S. M. R. Jarchavi, A. Zaidi, A. I. Najam, A. A. Alotaibi, A. Althobaiti, and S. S. Ghoneim, "Design and characterization of compact broadband antenna and its mimo configuration for 28 ghz 5g applications," *Electronics*, vol. 11, no. 4, p. 523, 2022.
- [66] N. E. h. Nasri, M. EL GHZAOUI, S. Das, T. Islam, W. Ali, and M. Fattah, "A novel arc-shaped four-port wideband (21.8–29.1 ghz) mimo antenna with improved characteristics for 5g nr networks," *International Journal of Communication Systems*, vol. 37, no. 7, p. e5746, 2024.
- [67] M. E. Munir, M. M. Nasralla, and M. A. Esmail, "Four port tri-circular ring mimo antenna with wide-band characteristics for future 5g and mmwave applications," *Heliyon*, vol. 10, no. 8, 2024.
- [68] N. Sghaier, A. Belkadi, I. B. Hassine, L. Latrach, and A. Gharsallah, "Millimeter-wave dual-band mimo antennas for 5g wireless applications," *Journal of Infrared, Millimeter, and Terahertz Waves*, vol. 44, no. 3, pp. 297–312, 2023.
- [69] R. N. Tiwari, D. Sharma, P. Singh, and P. Kumar, "A flexible dual-band 4 × 4 mimo antenna for 5g mm-wave 28/38 ghz wearable applications," *Scientific Reports*, vol. 14, no. 1, p. 14324, 2024.
- [70] M. F. Ahmed, M. I. Ahmed, A. A. Ibrahim, and S. M. Gaber, "Quad-port 28/38 ghz antenna with isolation improvement for 5g wireless networks," *Journal of Infrared, Millimeter, and Terahertz Waves*, vol. 45, no. 7, pp. 672–693, 2024.
- [71] R. N. Tiwari, D. Sharma, P. Singh, and P. Kumar, "Design of dual-band 4-port flexible mimo antenna for mm-wave technologies and wearable electronics," *IEEE Access*, 2024.
- [72] A. Azari, A. Skrivervik, and H. Aliakbarian, "A mmwave low complexity and low-cost super wideband dual-polarized aperture coupled antenna for 5g applications," *Ieee Access*, 2024.
- [73] D. Khan, A. Ahmad, and D.-Y. Choi, "Dual-band 5g mimo antenna with enhanced coupling reduction using metamaterials," *Scientific Reports*, vol. 14, no. 1, p. 96, 2024.
- [74] D. A. Sehrai, M. Asif, J. Khan, M. Abdullah, W. A. Shah, S. Alotaibi, and N. Ullah, "A high-gain and wideband mimo antenna for 5g mm-wave-based iot communication networks," *Applied Sciences*, vol. 12, no. 19, p. 9530, 2022.
- [75] K. Raheel, A. W. Ahmad, S. Khan, S. A. A. Shah, I. A. Shah, and M. Dalarsson, "Design and performance evaluation of orthogonally polarized corporate feed mimo antenna array for next-generation communication system," *IEEE Access*, 2024.
- [76] D. A. Sehrai, M. Asif, N. Shoaib, M. Ibrar, S. Jan, M. Alibakhshikenari, A. Lalbakhsh, and E. Limiti, "Compact quad-element high-isolation wideband mimo antenna for mm-wave applications," *Electronics*, vol. 10, no. 11, p. 1300, 2021.
- [77] Z. Cai, Y. Zhou, Y. Qi, W. Zhuang, and L. Deng, "A millimeter wave dual-lens antenna for iot-based smart parking radar system," *IEEE Internet of Things Journal*, vol. 8, no. 1, pp. 418–427, 2020.
- [78] R. Hussain, "Shared-aperture slot-based sub-6-ghz and mm-wave iot antenna for 5g applications," *IEEE Internet of Things Journal*, vol. 8, no. 13, pp. 10 807–10 814, 2021.
- [79] N. Hussain and N. Kim, "Integrated microwave and mm-wave mimo antenna module with 360 pattern diversity for 5g internet of things," *IEEE Internet of Things Journal*, vol. 9, no. 24, pp. 24 777–24 789, 2022.
- [80] X. Yang, Y. Ji, J. Hu, L. Ge, Y. Li, and K. M. Luk, "Wideband quasi-spherical lens antenna module with 2-d switched beams for 5g millimeter-wave iot applications," *IEEE Internet of Things Journal*, vol. 11, no. 1, pp. 1217–1227, 2023.
- [81] W. Song, G. Gourley, K. Zhao, J. Zhang, G. Goussetis, Z. Yi, and L. Wang, "A millimeter-wave shared-volume dual-aperture antenna array with enhanced spatial coverage efficiency for iot devices," *IEEE Internet of Things Journal*, vol. 12, no. 13, pp. 25 381–25 392, 2025.
- [82] D. Wang, L. Cao, W. Shen, Z. Li, and Q. Li, "Age of information minimization in aerial irs assisted covert communication for internet of things networks," *IEEE Internet of Things Journal*, 2025.
- [83] S. Sun, G. R. MacCartney, and T. S. Rappaport, "Millimeter-wave distance-dependent large-scale propagation measurements and path loss models for outdoor and indoor 5g systems," in *2016 10th European*

conference on antennas and propagation (EuCAP). IEEE, 2016, pp. 1–5.

- [84] G. Caso, Ö. Alay, L. De Nardis, A. Brunstrom, M. Neri, and M.-G. Di Benedetto, "Empirical models for nb-iot path loss in an urban scenario," *IEEE Internet of Things Journal*, vol. 8, no. 17, pp. 13 774–13 788, 2021.
- [85] S. Sun, T. S. Rappaport, T. A. Thomas, A. Ghosh, H. C. Nguyen, I. Z. Kovacs, I. Rodriguez, O. Koymen, and A. Partyka, "Investigation of prediction accuracy, sensitivity, and parameter stability of large-scale propagation path loss models for 5g wireless communications," *IEEE transactions on vehicular technology*, vol. 65, no. 5, pp. 2843–2860, 2016.
- [86] G. R. Maccartney, T. S. Rappaport, S. Sun, and S. Deng, "Indoor office wideband millimeter-wave propagation measurements and channel models at 28 and 73 ghz for ultra-dense 5g wireless networks," *IEEE access*, vol. 3, pp. 2388–2424, 2015.



Hassan Zakari was born in Rome, Italy, in 1996. He obtained the M.Sc. degree (Hons.) in Electrical Engineering from Amirkabir University of Technology (Tehran Polytechnic) in 2021. He is currently pursuing a Ph.D. in the Electromagnetic Research Laboratory of the Electrical Engineering Department at Amirkabir University of Technology. His research interests include Microwave Photonic, Antennas, terahertz devices and applications, optical fiber, 5G/6G and beyond wireless communications, and multiple-input multiple-output (MIMO) systems.



Gholamreza Moradi (Senior Member IEEE) received his BSc degree from the University of Tehran in 1989, and Ph.D. degree in electrical engineering from Amirkabir University of Technology (Tehran Polytechnic), Tehran, Iran in 2002. His main research interests are high-frequency characterization of materials, numerical Electromagnetics, microwave imaging, and planar microwave/mm-wave and THz systems. From 1997 to 2005, Dr. Moradi served as a faculty member and head of the research department at the Civil Aviation Technology College

in Tehran, Iran. There, as a two-year project, he developed a standardized training package approved by CAO. He was on a sabbatical leave at the University of Alberta from June 2016 to February 2016. He has also collaborated on research with the University of Dresden. Prof. Moradi has conducted numerous research projects on active microwave circuits, planar antennas, 5G wave propagation modeling, bioimplants, and high-frequency measurement techniques. During the past two decades, he has supervised more than 10 PhD candidates, 60 MSc and 90 BSc students. Also, he has acted as referee for over 250 graduate students. He has served on the promotion committee for lecturers at various universities. Dr. Moradi is the vice-chair of the Electromagnetics and Photonic Society of the IEEE Iran section. Dr. Moradi has authored over 10 books in his specialty; among them, "Active Transmission lines" won the National Book of the Year Award in 2008. He has published and presented almost 200 papers in refereed journals and international conferences. He serves as a reviewer for many IEEE journals, other highly reputable periodicals, and international conferences. He is one of the co-founders of the MMWaTT conferences. Gholamreza Moradi has taught and worked in various universities, including Iran University of Science and Technology, Air Science University, Islamic Azad University, and the University of Sistan and Baluchestan. He is currently a Professor in the Department of Electrical Engineering at Amirkabir University of Technology.



Mohammad Alibakhshikenari (Member, IEEE) (Member, IEEE) was born in Mazandaran, Iran, in February 1988. He received the Ph.D. degree with the European label and Excellent Cum Laude in electronics engineering from the University of Rome "Tor Vergata" (UNITOV), Italy, in February 2020. From May 2018 to December 2018, he was a Ph.D. Visiting Researcher with the Chalmers University of Technology, Gothenburg, Sweden. His training during this visit included a research stage at the Swedish Company "Gap Waves AB." During his

Ph.D. (Nov. 2016 - Feb. 2020), he was recognized as the winner of 13 grants for attending the Doctoral Schools organized by ESoA (European School of Antennas, 5), EUPROMETA (European Doctoral Programmes in Metamaterials, 3), EuMC (European Microwave Conference, 2), SIE (Società Italiana di Elettronica - Italian Society of Electronics, 1), ITMO University (Nanophotonics and Metamaterials, 1), Aix-Marseille Université (Metamaterials, 1), which were held in various European universities. He successfully completed all 30 credits required by the Doctoral Schools, earning his Ph.D. degree with a European label. He is now a Marie Skłodowska-Curie, ROSETTA, and LERO (the Research Ireland Centre for Software) Fellow at the University of Galway, Ireland. As part of this fellowship, he had five research visits at the Microwave Engineering Center for Space Applications (MECSA, October 2025); Universitat Ramon Llull, Barcelona, Spain (October 2025); Institute of Science Tokyo, Japan (November 2025); Pusan National University, Busan, South Korea (December 2025); and Sogang University, Seoul, South Korea (December 2025). From September 2024 to June 2025, he was with UNITOV as a Senior Researcher. From July 2021 to August 2024, he was with the Department of Signal Theory and Communications, Universidad Carlos III de Madrid (UC3M), Spain, as a Marie Skłodowska-Curie and CONEX-Plus Fellow. During this Program he has spent two secondments at the: 1) Microwave Engineering Center for Space Applications (MECSA), Rome, Italy, from April to August 2024, and 2) SARAS Technology Ltd., Company, Leeds, U.K., from December 2022 to May 2023. In addition, during this program he had one-week research visits at the: 1) University of Catania, Italy, in May 2024, along with an invited lecture entitled "Terahertz Antennas based on Metasurface and SIW" for the master's and Ph.D. students, and postdoctoral researchers; 2) University of Messina, Italy, in May 2024; 3) University of Bradford, U.K., in May 2023; and 4) Edinburgh Napier University, U.K., in April 2023. For the academic years 2021 and 2022, he received the "Teaching Excellence Acknowledgement" certificate for the course "electromagnetic fields" from the Vice-Rector of Studies at UC3M. In November 2019, he was the winner of a two-year postdoctoral research fund awarded by UNITOV. His research interests include "Electromagnetic fields, antennas and wave-propagations, metamaterials and metasurfaces, RF and microwave technologies, sensors, wireless communications, multiple input multiple output (MIMO) systems, millimeter-waves and terahertz integrated circuits, gap waveguide technology, and beamforming networks". His research activities are documented in about 200 papers published in international journals, 1 book, 9 book chapters, and about 112 papers in the proceedings of international conferences, including 49 in-person presentations at 31 conferences and 27 online presentations at 13 conferences (the rest were presented by my colleagues). His research papers have received more than 9000 citations, with an H-index above 58, as reported by Scopus, Google Scholar, and ResearchGate. According to Stanford University's annual analysis, he has been among the World's Top 2% of highly cited scientific authors since 2020. He was listed in both the Career Long and Single Year Impact sections of Stanford's list. He was a recipient of two Young Engineer Awards of the 47th and 48th European Microwave Conferences held in Nuremberg, Germany, in 2017, and in Madrid, Spain, in 2018, respectively. In April 2020, his research article entitled "High-Gain Metasurface in Polyimide On-Chip Antenna Based on CRLH-TL for Sub Terahertz Integrated Circuits, published in Scientific Reports, volume 10, Article number 4298 (2020)" was awarded as the Best Month Paper at the University of Bradford, U.K. In addition, he serves as an Associate Editor for two scientific journals, Radio Science and The Journal of Engineering (IET). He serves as a referee for several journals and as a member of the technical program committee (TPC) and session chair for several international conferences. In addition, he is a member of the reviewer panel of the Dutch Research Council (NWO), the U.K. Research and Innovation (UKRI) Funding Service, the IEEE MTT-S Education Committee Fellowships and Scholarships, and the External Examiner for several Ph.D. dissertations from various universities worldwide.



BAL S. VIRDEE (Senior Member, IEEE) received the B.Sc. and M.Phil. degrees in communications engineering from the University of Leeds, U.K., and the Ph.D. degree in electronic engineering from the University of London, U.K. He has worked in industry for various companies, including Philips, U.K., as a Research and Development Engineer, and Teledyne Defence and Space as a Future Products Developer in RF/microwave communications. He has taught at several academic institutions before joining London Metropolitan University, where he is

currently a Senior Professor in communications technology with the School of Computing and Digital Media and also the Head of the Communications Technology Research Center. His research, in collaboration with industry and academia, is in wireless communications encompassing mobile phones to satellite technology. He has chaired technical sessions at IEEE international conferences and published numerous research papers. He is an Executive Member of the IET's Technical and Professional Network Committee on RF/Microwave Technology. He is a fellow of the IET.



Chan Hwang See (M'14, SM'15) received a first class B.Eng. Honours degree in Electronic, Telecommunication and Computer Engineering and a Ph.D. degree from the University of Bradford, UK in 2002 and 2007, respectively. He is a Professor of Antennas and Applied Electromagnetics in the School of Computing, Engineering and the Built Environment, Edinburgh Napier University, UK. From 2019-2022, he was the Head of Electrical Engineering and Mathematics at the same institution. His research interests cover wireless sensor network system design,

computational bioelectromagnetics, antennas, microwave circuits, Internet of Things (IoTs), microwave sensors, Wireless Power Transfer (WPT), and microwave energy harvesting. He has published over 300 peer-reviewed journal articles and conference papers in these research areas. He is a co-author for one book and three book chapters. Since 2023, he has served as the UK representative for Commission K: Electromagnetics in Biology and Medicine within the International Union of Radio Science (URSI). Dr. See received the IEEE Malaysia AP/MTT/EMC Joint Chapter Best Paper Award in 2020. He was a recipient of two Young Scientist Awards from the International Union of Radio Science (URSI) and Asia-Pacific Radio Science Conference (AP-RASC) in 2008 and 2010, respectively. He was awarded a certificate of excellence in 2009 for his successful Knowledge Transfer Partnership (KTP) with Yorkshire Water, for the design and implementation of a wireless sensor system for sewerage infrastructure monitoring. Dr. See is a Chartered Engineer, Fellow of the Institution of Engineering and Technology. He is also a Fellow of the Higher Education Academy, a full member of the EPSRC Review College, an Associate Editor for IEEE Access, and an Editor for Journal of Electronics and Electrical Engineering, Scientific Reports, PeerJ Computer Science, Frontiers in Antennas and Propagation-Metamaterial Antennas and Wireless Power Transfer Journals. According to Web of Science, he has completed over 500 verified reviews and over 350 verified editor records.



Slawomir Koziel (Fellow, IEEE) received the M.Sc. and Ph.D. degrees in electronic engineering from the Gdansk University of Technology, Poland, in 1995 and 2000, respectively, and the M.Sc. degree in theoretical physics and the M.Sc. and Ph.D. degrees in mathematics from the University of Gdansk, Poland, in 2000, 2002, and 2003, respectively. He is currently a Professor in the Department of Technology at Reykjavik University, Iceland. His current research interests include the CAD and modeling of microwave and antenna structures, simulation-driven

design, surrogate-based optimization, space mapping, circuit theory, analog signal processing, evolutionary computation, and numerical analysis.